

Moving Beyond Compliance in Soft-Robotic Catheters Through Modularity for Precision Therapies

B. Calm  *, N. J. Greenidge, A. Metcalf, A. Bacchetti, G. Loza, D. Kpeglo, P. Lloyd, V. Pensabene, J. H. Chandler, P. Valdastri

Affiliations:

STORM Lab, University of Leeds, Leeds, United Kingdom.

School of Electronic and Electrical Engineering and Pollard Institute, University of Leeds, Leeds, United Kingdom.

Leeds Institute of Medical Research at St James' University Hospital, University of Leeds, Leeds, United Kingdom.

*Corresponding author. Email: b.p.calme@leeds.ac.uk

Abstract: Soft robotic systems offer promising solutions for navigating delicate, tortuous anatomy, but clinical adoption has been hindered by limited functionalization and insufficient real-time feedback at the instrument tip, the critical interface for tissue interaction. Although compliant materials and embodied intelligence have enabled millimeter-scale access, few sensing and functionalization approaches are sufficiently compact, robust and adaptable to measure, and respond, to subtle physiological cues during intraluminal procedures.

We present a 1.47-mm-diameter modular soft robotic catheter that integrates sensing, actuation, and therapeutic capabilities while retaining the compliance needed for safe endoluminal navigation. Although validated in multiple *in vivo* settings, we highlight the robot's utility in endoscopic retrograde cholangiopancreatography (ERCP), one of the most technically challenging endoluminal procedures and a key access route to the pancreas, an organ that remains fragile, difficult to instrument, and central to diseases such as pancreatic cancer, which continues to show poor survival outcomes.

Our modular architecture supports up to four independently controlled functional units, enabling customizable combinations of anchoring, manipulation, sensing, and targeted drug delivery. In a live porcine model, we demonstrate semi-autonomous deployment into the pancreatic duct and 7.5 cm of endoscopic navigation into the pancreatic duct, a region currently inaccessible with standard catheters. A closed-loop autonomous/shared-control system, combining a learned model, magnetic actuation, onboard shape sensing, and visual marker tracking, further enhances cannulation accuracy.

This work establishes a scalable platform for multifunctional soft robotic catheters and introduces a new paradigm for complex endoluminal interventions, with the potential to reduce radiation exposure, shorten training requirements, and accelerate the clinical translation of soft robotic technologies.

One-Sentence Summary: Modular soft magnetic robotic catheter enables multifunctional, autonomous navigation and therapy in millimeter-scale anatomy

INTRODUCTION

Soft robotics offers a compelling alternative to traditional rigid-bodied systems for navigating complex and delicate anatomy [1], [2]. The inherent compliance of soft robotic systems allows safe interaction with tissue, making them attractive for minimally invasive procedures where precision and safety are critical. Recent advances in stretchable electronics, soft actuation, and control theory have enabled devices that withstand extreme strains ($>300\%$) and achieve motion intelligence despite nonlinear, rate-dependent dynamics [3], [4], [5]. Yet, much of the field's progress has centered on navigation and tip steerability, leaving a persistent gap between proof-of-concept soft robots and clinically viable platforms capable of performing full procedures.

Actively steerable catheters based on tendon-driven, concentric tube, or fluidic architectures can achieve large deflections but suffer from friction, hysteresis, and nonlinear backlash that limit accuracy and repeatability [6]. Magnetic soft continuum robots (mSCRs) overcome these transmission losses by enabling wireless actuation and improved dexterity [7], [8]. The high remanence of hard-magnetic materials allows them to retain high residual magnetic flux density even in the absence of magnetic fields once they are magnetically saturated. In addition, the high coercivity of hard-magnetic materials helps them sustain the high residual magnetic flux density over a wide range of applied magnetic fields below the coercive field strength. By embedding hard-magnetic microparticles, e.g., NdFeB (neodymium-iron-boron), into soft elastomers, these devices can undergo programmable magnetization for complex shape reconfigurations [9], [10], [11], [12] in response to external fields while preserving compliance. But most mSCRs that have been demonstrated focus on neurovascular [7], [8], [13], pulmonary [14], and reproductive system [15] interventions, and remain limited to navigation tasks. Studies have demonstrated laser-ablation ability [14], in situ biosensing [16] and printing [17], or carrying micro-robot [18], [19], but to move toward clinical translation, mSCRs must integrate additional functions - imaging, anchoring, manipulation, therapy delivery - without compromising on their softness or miniaturization.

This challenge is particularly acute in endoscopic retrograde cholangiopancreatography (ERCP), a technically demanding procedure targeting the pancreaticobiliary system. The global burden of pancreatic cancer has more than doubled in recent decades. It is now the sixth leading cause of cancer-related death worldwide and remains one of the deadliest malignancies with an overall five-year survival rate of 10% worldwide [20]. Despite progress with technology such as with the SpyScope (Boston Scientific, USA), diagnostic and therapeutic access to the pancreatic duct is limited by the stiffness and diameter mismatch, which require trauma (sphincterotomy) and cannot easily accommodate multiple tools [21]. Moreover, the current procedure requires a specific endoscope with a side view, the duodenoscope, complicating the navigation down to the duodenum. As a result, ERCP procedures are technically demanding for the operator and tend to generate long-term side effects and complications for the patient, motivating the need for softer, multifunctional, and controllable tools.

Here, we present a 1.47 mm outer-diameter modular soft robotic catheter that combines magnetic steerability with multi-functionality while preserving compliance for safe navigation. Our platform is hardware-agnostic, being deployable through standard clinical tools and actuated via any magnetic manipulation system, either using permanent or electro-magnet. The device can be configured with up to four independent functional modules, including onboard imaging, a tendon-driven compliant gripper, tunable magnetic anchoring balloons, and ultrasound-triggered drug-release coatings. Each module is designed and optimized to function both on its own and together with the others. We introduce a scalable manufacturing process that integrates 100 μm microchannels, illumination, and customizable balloon geometries into a monolithic body.

We validate this system in live porcine models, demonstrating semi-autonomous cannulation of the pancreatic duct, secure anchoring with targeted drug delivery, and 75 mm of navigation to the distal bile duct, beyond the reach of standard catheters and clinically relevant to ~50–60% of

pancreatobiliary tumors [22]. Finally, we implement a closed-loop control strategy coupling onboard shape sensing and real-time tracking based on a convolutional neural network model, for autonomous insertion, reducing operator burden while preserving anatomical papilla integrity.

By moving beyond compliance and enabling precision therapy through modularity and autonomy, this work establishes a new paradigm for soft robotic catheters: not only navigating anatomy safely but also delivering clinically actionable functions for diagnosis and therapy.

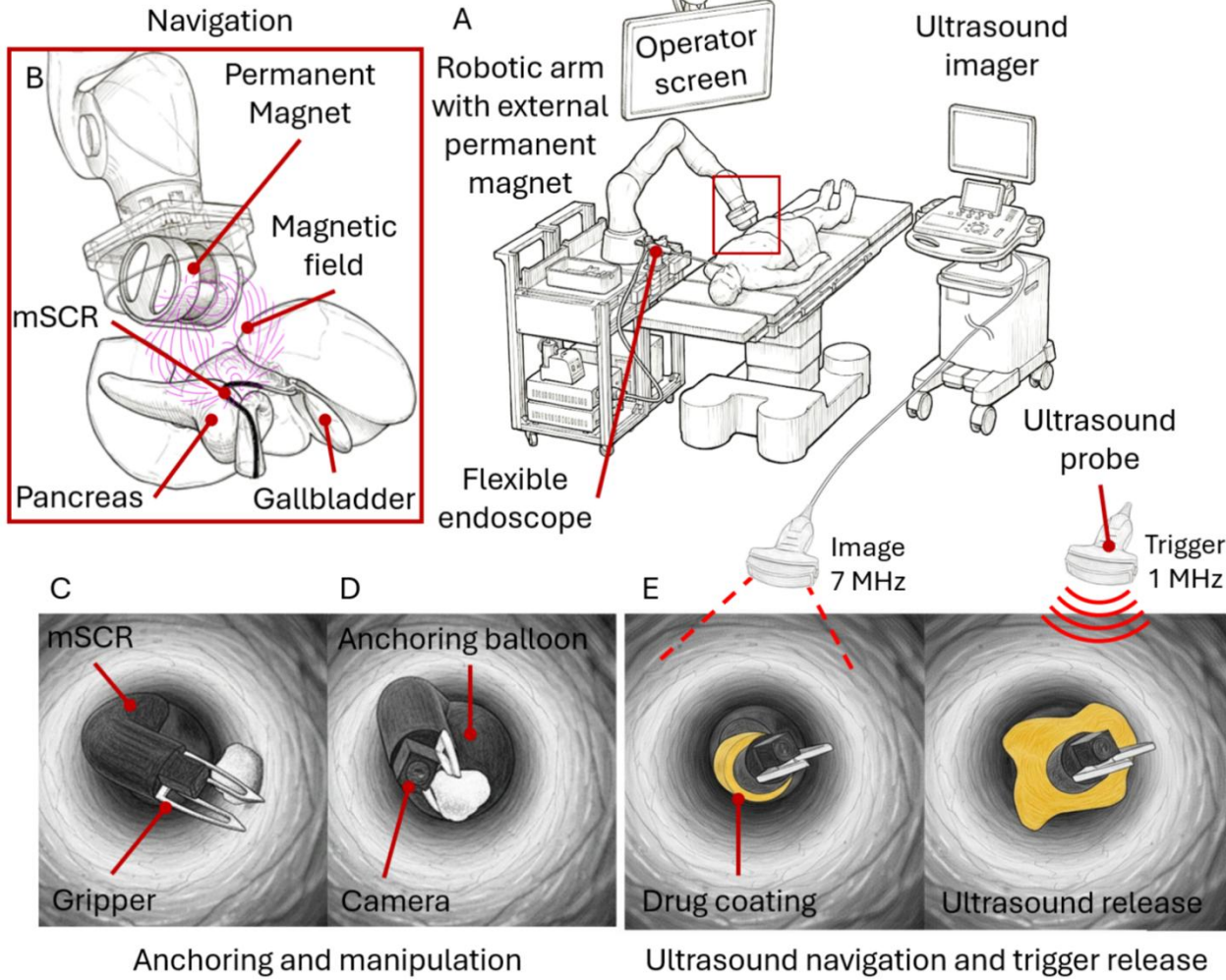


Figure 1 Robotic platform for millimeter-scale modular mSCR enabling precise medical procedures. (A) Platform setup during the trials. (B) Illustration of magnetic navigation: an external permanent magnet is used to steer the magnetic catheter inside the pancreatic duct. (C) Functionalized mSCR anchored in the duct, enabling direct visualization and (D) retrieval of objects obstructing the lumen. (E) Ultrasound-guided navigation and drug release for targeted therapy.

RESULTS

Robotic platform overview

Building upon prior work on mSCR design and control [14], [23], we developed a miniaturized, multifunctional mSCR that combines robust magnetic steerability with three functional modules: a compliant gripper, a hyperelastic magnetic anchoring balloon, and a micro-patterned biocompatible polylactic acid (PLA)-coating for ultrasound-triggered drug release. The catheter body integrates 100- μ m microchannels, a miniature camera with LED illumination, and markers for pose estimation, all within the 1.47-mm outer diameter (movie_S1). This device is designed to directly address the central limitations of earlier designs, delivering useful clinical functions at the target site.

Magnetic actuation was achieved by a large external permanent magnet (EPM) mounted onto a 7-DOF robotic manipulator positioned at the patient's bedside (Fig. 1A). The EPM was placed 18 cm above the patient chest, with software-defined motion limits to ensure patient safety (Fig. S1).

To achieve these limits, the reachable workspace of the robotic manipulator, defined as the set of positions in space that can be reached by its end-effector, is constrained using the magnetic-feasible workspace [24], defined as the set of positions where a desired set of magnetic tasks is feasible for a given end-effector position. The typical desired task was $D = \{\mathbf{B} \in \mathbb{R}^3 | 16 \leq |\mathbf{B}| \leq 25\}$, which can be achieved within a workspace of 0.05 m^3 with field strength up to $|\mathbf{B}| = 25 \text{ mT}$ on the mSCR, sufficient to generate tip torques of up to $\tau = 6.72 \text{ N}\cdot\text{m}$ (Fig. 1B).

The operator interface integrates two joysticks (one for EPM pose, one for module actuation), an automated advancing unit for feed/retraction, and a computer-controlled insufflation system. All subsystems run under Robot Operating System (ROS), enabling modular control and synchronized data streaming.

Using onboard first-person video, the mSCR navigated 75 mm into the pancreatic duct (Fig. 1B). Demonstration of navigation was also validated a second time through the exploration of multiple segmental pulmonary branches (movie_S2). The onboard camera improved operator situational awareness and provided a clear view of the gripper–tissue interface (Fig. 1C, D). The operator can displace objects of different shapes and textures. The gripping force can be increased by a factor of 2.5 by simultaneously using the anchoring balloon (Fig. 1D) or use the latter to stabilize the mSCR while performing ultrasound-triggered drug delivery (Fig. 1E).

During deployment, a flexible endoscope is advanced to the duodenum to visualize the major and/or minor papilla (Fig. 2E). The papillae are small mucosal openings in the duodenum where the bile and pancreatic ducts empty, delivering bile and digestive enzymes into the intestinal lumen. The endoscope is then secured on a bedside support to stabilize the visual field. Our workflow was successfully validated on three endoscopes across two distinct magnetic actuation setups (Fig. S3, S4 and Table S1), demonstrating hardware agnosticism and compatibility with standard clinical tools.

To ease the most delicate stage of the procedure, the cannulation of the papilla, we implemented a degree of machine intelligence by providing an autonomous insertion strategy. This was demonstrated with a mean insertion time of $t = 223 \pm 10 \text{ s}$ across two porcine models, compared to $t = 253 \pm 23 \text{ s}$ when the system was controlled by an operator.

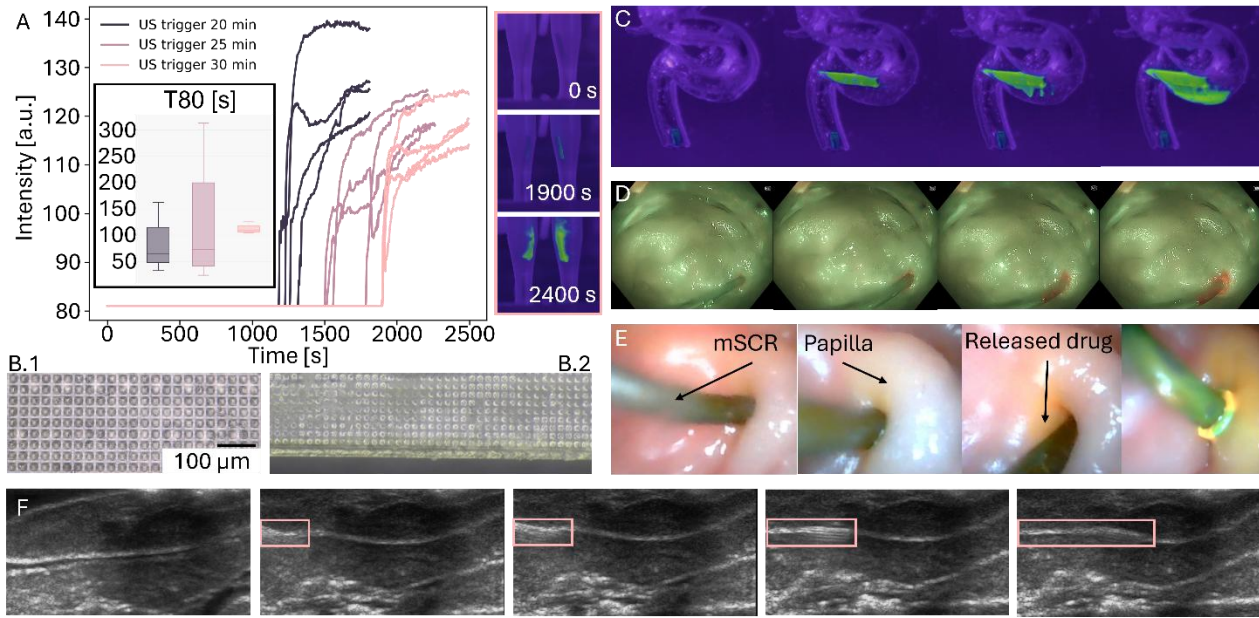


Figure 2 Ensuring safe navigation and targeted drug delivery using ultrasound. (A) Bench-top validation of the approach, showing precisely timed drug release with representative snapshots; performance is quantified using the 80% release time (T_{80}) for each sample batch. (B) The mold (1) was 3D-printed, coated with drug-doped PLA by spin coating (2), and used to fabricate the shell that is subsequently assembled onto the mSCR. (C) Controlled drug release in an aneurysm phantom. (D) Ex vivo assessment of drug release using narrow-band imaging. (E) In vivo demonstration of drug release in the pancreatic duct. (F) In vivo ultrasound validation of mSCR deployment inside the pancreatic duct.

PLA-shelled, ultrasound-triggered drug release

In this work, we use unfocused ultrasound (US) for the dual purpose of real-time imaging (typically 7–28 MHz) and to drive mechanically triggered release from polymer shells. We initially started from an approach using electrospun fabrics [25], but the end-size and the process were not compatible with the functionalization required for the procedure. Therefore, the design and fabrication approach changed to produce a micrometer-thick PLA coating around the mSCR with a designed micropattern (squares, 20 μm edge length, 5 μm depth, 10 μm spacing; Fig. 2.B) whose dominant mode resonates near 1 MHz. This frequency was selected to avoid overlapping with imaging US and to leverage deeper tissue penetration. The coating remains inert under imaging ultrasound, but fractures under 1 MHz actuation, releasing the payload on demand. The pattern on the molded shell had an area of $401.7 \pm 24 \mu\text{m}^2$, validating the molding approach (400 μm^2 expected) (Fig. S5).

After finite-element modal analysis to confirm the 1 MHz natural frequency (Fig. S11), we demonstrated its proper functioning in vitro and in vivo. In vitro, we demonstrated time-controlled release: samples were continuously stimulated at 7.2 MHz to simulate imaging and at pre-specified times (20, 25, 30 min) a 1 MHz frequency was applied, and release was visually confirmed (Fig. 2A, movie_S3). Release experiments showed a payload release of 80% within $t = 104 \pm 22$ s after 1 MHz insonation ($n = 4$, $N=12^1$), with no measured leakage during baseline imaging.

Phantom and ex vivo studies demonstrated optical confirmation of release using narrow-band endoscopic imaging (415 nm) (Fig. 2C, D). In vivo trials validated successful on-demand release after navigation across the bile duct (Fig. 2E), as well as in the gastrointestinal tract and the lung (Fig. S6), with performance robust to pH and hydration changes. Contact with tissue, in the absence of media, is required to couple ultrasound energy into the shell. During the procedure, the catheter

¹ n represents the sample size, when N represent the total number of repetitions

was tracked in real time while navigating the biliary duct using the imaging ultrasound transducer without pre-mature drug release (Fig. 2F, Fig. S2).

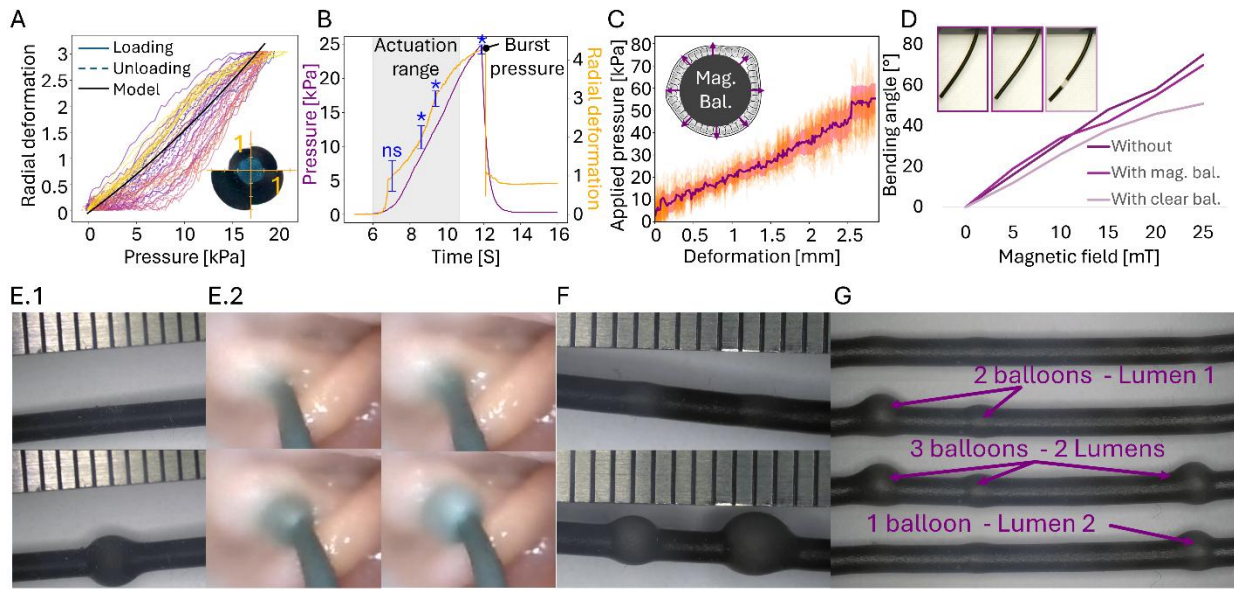


Figure 3 Providing stability using an anchoring hyperelastic magnetic balloon. (A) Model-predicted large strain magnetic balloon. (B) Full characterization of the balloon up to bursting and definition of the safe actuation range for the actuation unit. (C) Radial pressure applied by the balloon (Mag. Bal.) on the surrounding tissue to anchor the mSCR, shown as a function of deformation. (D) Demonstration that the presence of a magnetic balloon does not affect mSCR deformation compared with a non-magnetic balloon (clear bal.). (E) Single-balloon configuration, shown on the bench and in vivo. (F) Validation of the fabrication of two interconnected balloons with different geometric properties. (G) Demonstration of the fabrication of a three-balloon mSCR: two interconnected balloons with different geometric properties and one balloon with an independent lumen sharing the same geometric parameters as the first balloon.

Anchoring Hyper-Elastic Magnetic balloon

Inflatable actuators [26] are widely used in soft robotics for actuation [27], sensing [28], and navigation [29]; in slender catheters they also provide stabilization and improve force transmission. However, in the literature, soft balloons are described as susceptible to prismatic, axisymmetric, or asymmetric buckling during inflation, which compromise reliability [30]. We therefore derived a buckling-aware design framework to ensure predictable inflation under clinically relevant loads. Considering the large strains observed (>300%) (Fig. 3A), we employed a Yeoh strain-energy density function (preferable to lower-strain models) to link internal pressure, external tissue pressure, axial loads (from gripper actuation), and radial deformation (Fig. 3B and supplementary material 2).

The model demonstrates its reliability particularly in the higher range ($\text{RMSE}_{<10\text{kPa}} = 0.4 \text{ mm}$, $\text{RMSE}_{>10\text{kPa}} = 0.3 \text{ mm}$) deviation in pressure-deformation behavior compared to the experiment ($n = 3$, $N = 30$, Fig. 3B). The reliability of the manufacturing process is also assessed by the repeatability of the bursting pressure obtained during the characterization, allowing evaluation of a safety criterion dependent on the balloon in the actuation unit ($n = 3$, $N = 30$, Fig. 3C). Bench tests showed a mean applied pressure up to 57 kPa ($n = 3$, $N = 30$, Fig. 3C) and a holding force of $F_{\text{anchor}} = 3.3 \pm 0.2 \text{ N}$ ($n = 3$, $N = 30$) (Fig. S7), sufficient to stabilize the catheter within the biliary duct during gripper actuation and resist magnetic perturbations. Distal anchoring also allows for improved dexterity of the tip as it can be manipulated independently of the rest of the mSCR body. As the balloons are fabricated within the catheter's body, they can be magnetized along with the body such that, when deflated they maintain continuous magnetization, preserving compatibility with shape-forming strategies (Fig. 3D and Fig. S3,4). The framework supports both single (Fig. 3E) and multi-balloon configurations, with custom geometries (Fig. 3F) and independent or

simultaneous actuation (Fig. 3G). In vivo, the balloon achieved secure anchoring within the biliary duct (Fig. 3E2).

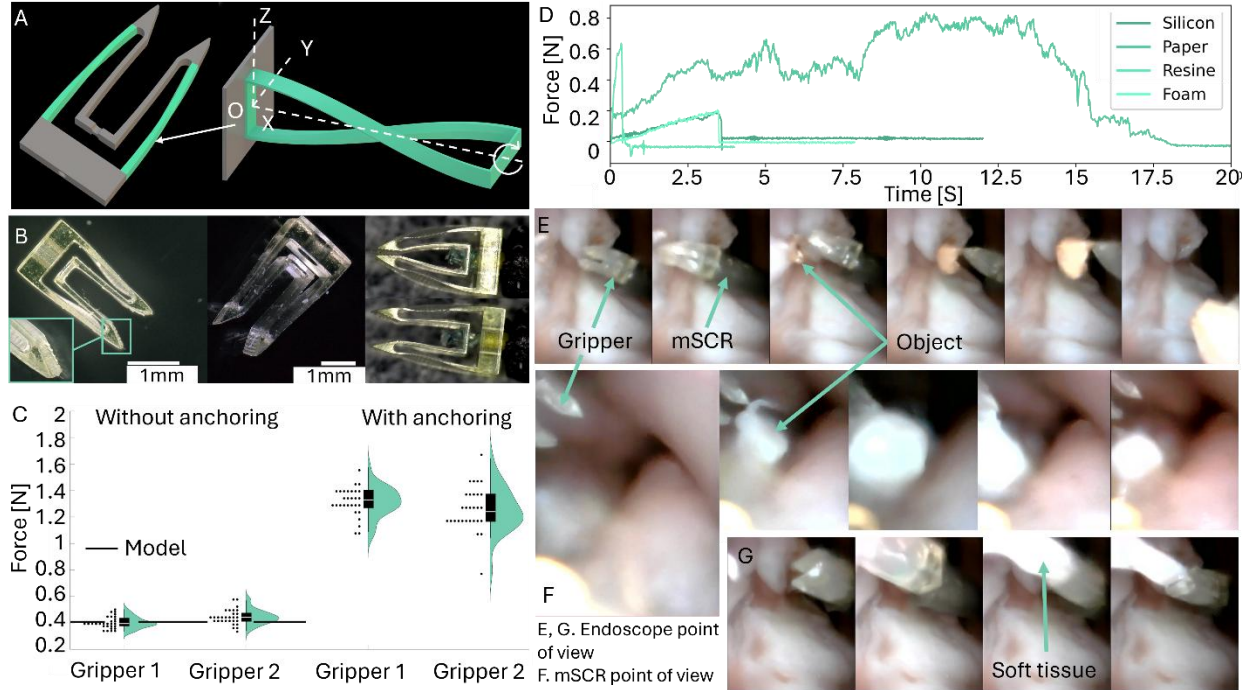


Figure 4 . Integration of an effective gripper in the mSCR for object manipulation. (A) Lateral blades of the compliant gripper are twisted to tune their natural frequency and prevent interference from ultrasound actuation. (B) Microscopic image of the 3D-printed gripper showing the jaw pattern, the nylon wire lumen, and the open and closed configurations. (C) Comparison between the model with gripper 1 (straight blades) and gripper 2 (45°-twisted blades) before and after balloon anchoring. (D) Characterization of gripping force on objects with different mechanical properties moving at 5 mm/s. (E) In vivo endoscopic view of the gripper collecting a rigid object. (F) In vivo mSCR-mounted camera view of the gripper during object manipulation. (G) In vivo endoscopic view during manipulation of soft tissue to expose it in front of the camera.

Compliant gripper

Compliant mechanisms commonly are monolithic structures that transmit motion and force through elastic deformation rather than discrete joints. Their geometry is optimized to distribute local strains, produce a desired shape change, and avoid stress concentrations. Our gripper is inspired by a flexure-based L-arm mechanism [31], [32] in which a central shuttle translates relative to a fixed base to close the jaws. In our embodiment, the base is bonded to the camera housing for precise co-axial alignment, and actuation is provided by pulling an 80 μ m nylon tendon.

To better capture the distributed deformation of the flexures and reduce distal body perturbations during closure, we adapted the gripper model from localized [32] to distributed compliance, and geometrically optimized the flexures accordingly. Furthermore, to avoid interference with ultrasound-triggered drug release (section below), the jaw blades incorporate a twisted design to shift their natural frequencies (Fig. 4A).

The flexure-based compliant gripper enabled reliable object and tissue grasping in bench and in vivo experiments (Fig. 4D–G). Geometric optimization of the flexures produced strong agreement between model predictions and measured jaw deflections and the triggering force with less than 7% deviation ($n = 30$ trials, Fig. 4C).

Peak gripping force without anchoring was 0.43 ± 0.06 N ($n=2$, $N=60$). When combined with the anchoring balloon, effective gripping force increased to 1.28 ± 0.16 N ($n=2$, $N=60$), a ~300% improvement (Fig. 4C). Across bench experiments, we demonstrated gripping forces with different materials and at different moving speeds (Fig. S8), and validated performance in vivo through reliable manipulation of objects and tissue (Fig. C and D) and object removal (movie_S4). Co-location of the gripper with the camera improved object targeting (Fig. 2F).

Magnetic steering and navigation

Open-loop control exploration

Beyond initial entry into the major papilla, ERCP typically relies solely on external imaging because conventional guidewires lack onboard visualization. This limitation is common across many procedures performed in small-diameter lumens. By integrating a NanEye camera and LED fiber within the mSCR (Fig. 5A), we enabled true first-person visual navigation without dependence on external imaging modalities such as X-ray, despite the device being radiopaque (Fig. S9). Using joystick-controlled magnetic manipulation, we validated navigation within the pancreatic duct, our primary target, reaching depths of up to 75 mm (Fig. 5B), and demonstrated deep pulmonary access down to the sixth-generation segmental branches (Fig. 3C, movie_S2).

Porcine anatomy differs slightly from the human anatomy, i.e., the pancreatic and biliary duct are not connected. It is therefore not possible to demonstrate the ability to choose in which duct the operator want to navigate. This possibility was then demonstrated *in vivo* during the lung navigation (Fig. 3D, movie_S2).

As noted previously, the onboard camera also provides a direct view of the gripper–tissue interface, enhancing manipulation accuracy (Fig. 4F).



Figure 5 Demonstration of mSCR functionalization and *in vivo* navigational capability (porcine model). (A) Handheld mSCR incorporating all functional modules, with highlighted features and colored video-tracking markers supporting autonomous closed-loop control. (B) Successful advancement of the catheter 75 mm into the pancreatic duct. (C) Controlled navigation to sixth-generation branches of the pulmonary airway tree. (D) *In vivo* lung navigation visualized from the bronchoscope, showing sequential steering into two distinct airway branches.

Video-based Autonomous magnetic steering

To reduce operator burden and handle the nonlinearities of magnetic actuation, we implemented an autonomous-control pipeline that couples a YOLOv8 detection algorithm, a magnetic steering model and a fiber Bragg grating (FBG) shape sensor. The detector identifies the papilla and two mSCR tip markers from endoscopic video and estimates the tip orientation. The detector achieved precision = 0.81, recall = 0.76, and F1 = 0.78 on a dataset combining phantom, *ex vivo* and *in vivo* images (n = 3800 images).

The angular error relative to the desired entry line is mapped to a desired deformation, which a dipole–dipole magnetic model converts into an EPM pose. Once the deformation induces the mSCR tip to point toward the papilla, the advancing unit deploys the mSCR. If misalignment reoccurs, since the depth remains unknown, the system pauses and realigns before resuming.

To ensure safety, a fiber Bragg grating sensor was also integrated inside the catheter and compared to the model's estimated orientation. The error stayed consistently below 2 degrees (Fig. 6E). The errors at the lowest angles came from the difficulty of correcting small angles *in vivo* due to the environment changes and the non-linearity of the magnetic field, while the errors at the highest angles came from the FBG sensor, which does not support sharp turns. During autonomous orientation control, operator override always remains available. User interrupts trigger safe holding, and, from that point, the system can either be resumed to continue after validation, switch to open

loop control mode, or adjusted by changing the robot configuration to move the magnet out of the operating field.

We compared human-operated versus autonomous insertion in a realistic phantom (Fig. 6A, B) and in vivo (Fig. 6C, D). Overall, repetitions and scenario mean time were very similar with an 11s difference between the human operator and the autonomous approach. It is however noticeable that for the human operator the variance was higher, consistent with learning effects and case-dependent use of tissue contact. In certain scenarios, the operator leveraged support from the surrounding tissue to assist insertion. However, in vivo, autonomy outperformed manual control, as navigation strategies relying on tissue contact were less transferable. Human-operated insertion was 58% slower, 253 ± 12 s compared to 223 ± 3 s (Fig. 6H), and exhibited more erratic EPM motion (Fig. 6F, G, S10).

Our approach also demonstrates cross-platform viability, working with both duodenoscopes and gastroscopes (Fig. 6H, movie_S2), potentially mitigating the need for a dedicated endoscope to perform ERCP. As demonstrated, both the operator and the autonomous strategy successfully completed the procedure.

Finally, through all trials, the papilla remained intact, and no bleeding was observed. The only observed effect was progressive dilation with repeated insertions.

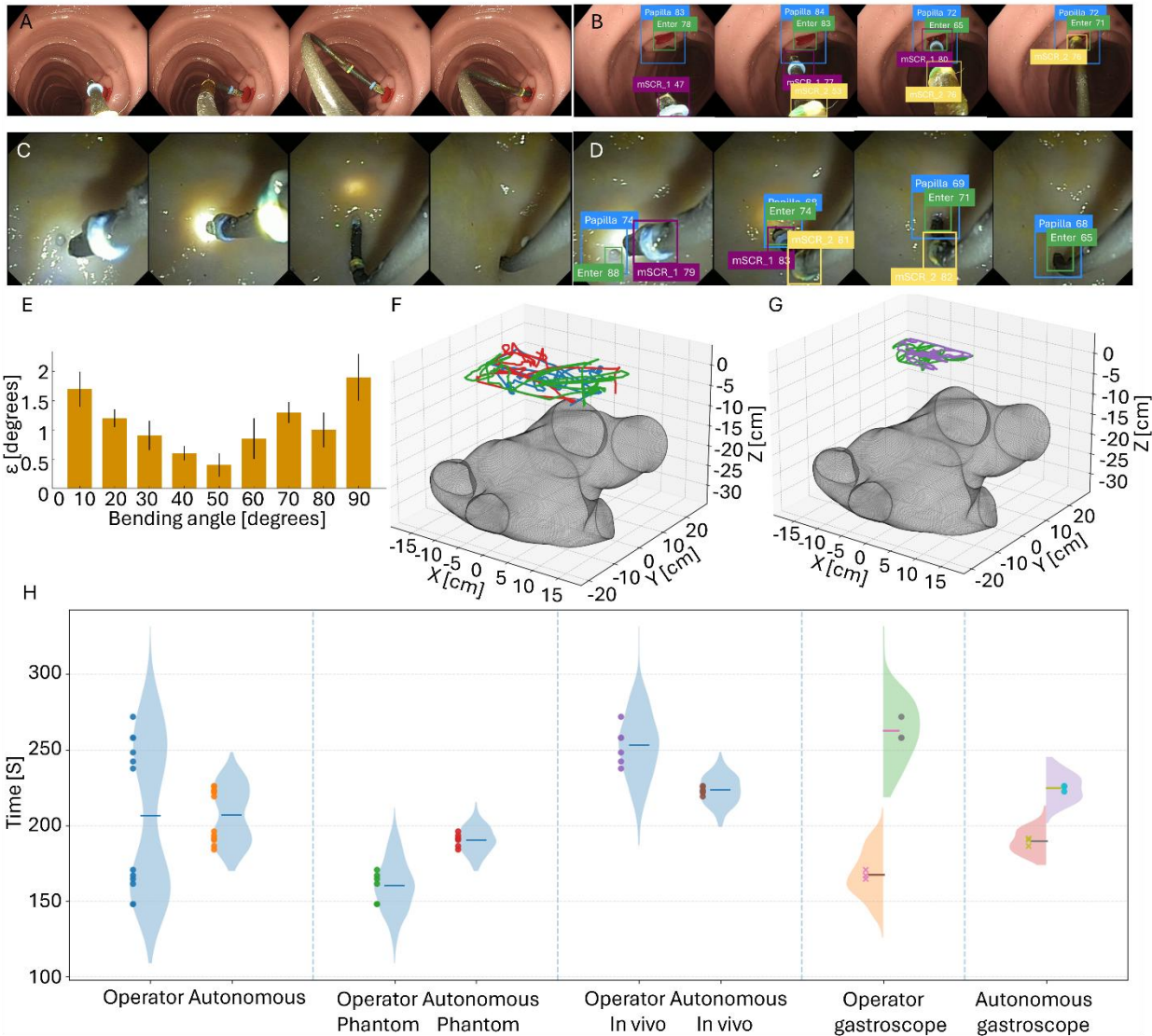


Figure 6 Providing Autonomous navigation to facilitate the insertion. (A) Operator-controlled navigation and insertion of the mSCR in a realistic phantom model. (B) Autonomous navigation and insertion in the same phantom. (C) Operator-controlled navigation in vivo. (D) Autonomous navigation in vivo. (E) Error between the model-estimated angular deformation and FBG-based measurements. (F) Displacement of the EPM across procedures, showing a more erratic trajectory under human operation. (G) EPM displacement during autonomous navigation, exhibiting a smoother and more consistent course. The meshed volume shown indicates the position of the pig's body during the trial. (H) Procedure time comparison between operator-led and autonomous cannulation, reported overall in the first column and across the following scenarios: phantom trials, in vivo experiments, and procedures performed with a gastroscope rather than a duodenoscope.

DISCUSSION

This work demonstrates that a magnetically steered soft continuum catheter (mSCR) with a 1.47 mm outer diameter, can deliver clinically relevant functions at the target while maintaining the compliance needed for safe intraluminal navigation. The platform integrates on-board imaging and illumination, a tendon-driven compliant gripper, tunable magnetic anchoring balloons, and ultrasound-triggered drug release. Crucially, it is platform-agnostic, deployable through standard endoscopes and compatible with different magnetic actuation systems. We validate the platform through the cannulation of the pancreatic duct (ERCP) in live porcine models, followed by secure anchoring and targeted delivery.

Our approach combines intuitive joystick steering with an autonomous control-loop pipeline that fuses endoscopic video with our orientation detection algorithm, validated by an FBG sensor, to perform the insertion. This intends to reduce operator burden during papilla cannulation while

preserving manual override. The result is a system that supports both exploratory open-loop navigation (enabled by on-board vision) and autonomous navigation for planned procedures. In addition, to enable deployment of current catheters, ERCP requires the use of a specialized endoscope with side-facing camera (duodenoscope). However, this makes general advancement towards the pancreas more challenging for the operator [33], [34]. By enabling deployment and cannulation through standard front-view endoscopes, our system simplifies navigation to the small intestine

The combination of an anchoring balloon and compliant gripper allows greater dexterity by improving distal force transmission and manipulation stability at the millimeter scale. The balloon's magnetizable construction preserves continuous magnetization when deflated (making it compatible with shape-forming) and provides atraumatic stabilization when inflated, thereby improving the effective gripping force. However, despite geometric optimization, transmitting force from the base to the tip still introduces some loss of precision. Distal actuation could improve accuracy without compromising compliance. One approach would be to integrate biohybrid actuators at the catheter tip [35], [36].

The micropatterned PLA shell provides on-demand therapeutic release under a 1 MHz acoustic trigger while remaining inert under standard imaging ultrasound (7–28 MHz), enabling targeted intervention without changing the imaging workflow. This approach implies releasing everything once triggered, which is not an issue when only a single cargo delivery is expected; if multiple deliveries are required, variable patterns could be envisaged, or other matrices with different natural frequencies or triggering mechanisms [37], [38].

Despite the capabilities demonstrated, several limitations remain. The current autonomous approach addresses tip alignment but lacks depth estimation; incorporating proper miniaturized localization system would shorten procedure time by reducing the number of readjustments. Such localization of the catheter would also enable real-time tracking of the catheter even once inside a lumen. Miniaturizing existing approaches described in [39], [40], could provide a long-term solution, albeit at the cost of additional cabling routed within the mSCR. An intermediate solution would be to adopt a vision-based approach using the mSCR's integrated camera, accepting the compromise of allocating a lumen for camera cleaning [41].

Using a single EPM to control a soft catheter brings challenges, as it involves greater non-linearity than coil- or dual permanent-magnet platforms [14], [19], which offer finer control. However, those platforms face space and access limitations in the operating theatre.

We demonstrate biocompatibility of our catheter, as we observed no harmful leachates during procedures; however, longer exposures could pose risks. Some reports note reduced metabolic activity after prolonged contact [42]. By demonstrating deep navigation within the pancreatic duct and repeated atraumatic cannulation of the papilla, this approach shows that a magnetic catheter can be used safely in a highly sensitive environment and, in the context of ERCP, potentially help reducing a major cause of long-term side effects for patients. The current ERCP approach can lead to acute pancreatitis and cholangitis in patients, which may worsen their condition and delay treatment or upfront surgery [43], [44], and [45].

By uniting magnetically enabled shape control with task-level functionality, imaging, manipulation, anchoring, and on-demand therapy, this platform advances soft robotic catheters towards practical clinical impact. We aim to reduce reliance on ionizing radiation, shorten the learning curve for complex navigation (e.g., ERCP), and provide a blueprint for procedure-specific modularity.

MATERIALS AND METHODS

Robotic platform

A 7-DoF kinematically redundant serial manipulator (LBR Med 14 R820, KUKA) carried a cylindrical N52 external permanent magnet (EPM) with a remanence of approximately 1.45 T and dimensions 100 mm in diameter by 100 mm thick. By adjusting the pose of the EPM relative to the patient, magnetic forces and torques were applied to the mSCR to achieve the desired shape changes (Section “Magnetic steering and navigation” and Fig. S3). Five different endoscopes were used successively during the trials, a duodenoscope, a gastroscope, a bronchoscope, and two different colonoscopes (Tab. S1). Endoscope video and the onboard camera feed were captured via a frame-grabber and streamed to the control computer for use in the control loop.

Two handheld joysticks (Nunchuck Controller, Nintendo, Japan) were used; one issued EPM pose commands and the other controlled catheter deployment and retraction as well as functional module actuation. A feed unit advanced the catheter, and a dedicated inflation unit controlled the balloon pressure. The setup during the clinical trials is presented in Fig. S1.

The platform is based on a Robotic Operating System (ROS), with networked nodes for: camera synchronization, feature detection and orientation estimation, manipulator control, motor drivers, FBG acquisition and shape reconstruction, user interface, and data storage.

mSCR actuation unit

The advancing unit comprised a five-phase hybrid stepper motor (MS17HV, MOONS') driven by a digital driver (2DM542, Just Motion Control) under an Arduino UNO R4 Minima. The motor was mounted on a lockable articulating base stage (SL20/M, Thorlabs) using a 3D printed adapter positioned at the endoscope inlet. The inflation unit used a lead screw linear module (drylin SAW 1080, igus) to actuate a 10 mL syringe through the same driver and microcontroller. A three-way stopcock connected the syringe to a pressure sensor (VSP1130, Amphenol) and the silicone inflation line to enable closed loop control. All electronics were enclosed in a safety housing with switching supplies (MPS KO-D120524V, Dynamic). Arduinos were operated as ROS nodes via rosserial over UART protocol: subscribers received joystick commands; publishers streamed pressure for closed-loop inflation to prevent over-pressurization and bursting, as well as the mSCR length deployed.

mSCR manufacturing process

Soft robotic catheter bodies were produced by low-pressure injection molding using high-resolution molds (microArch S140, Boston Micro Fabrication; HTL resin). Two-part shells incorporated integrated cores to define a 100 μm air channel and balloon lumen, together with guides for the camera, fiber, and tendon. The magneto-elastic matrix consisted of a 1:1 mass mixture of neodymium-iron-boron powder with 5 μm particles (MQFP-B+, Magnequench) and DragonSkin 30 silicone (Smooth-On, USA) that was mixed and degassed in a planetary mixer (Thinky ARE-250, Intertronics, UK) at 2000 rpm for 1.5 minutes, loaded into a syringe, and injected while vacuum venting removed trapped air. After curing, parts were released in an acetone bath; targeted acetone injection cleared sacrificial cores and confirmed lumen patency. The camera (NanEye, ams-OSRAM, USA), LED fiber (Thorlabs, USA), and multicore FBG (FBGs international, Belgium) were verified prior to integration. The compliant gripper was bonded co-axially to the camera housing and coupled to a nylon tendon. Finished catheters measured 1.45 ± 0.02 mm outer diameter and 80 mm length. The air channel was connected to a soft rubber tubing (0.3 mm ID and 0.64 mm OD, McMaster-Carr, IL, USA), then all the cables, fibers and tube were routed inside a medical grade PTFE tube (0.9 mm ID and 1.6 mm OD, McMaster-Carr, IL, USA). All the components can be quickly connected to their respective actuation unit before use.

mSCR magnetic manipulation

To successfully manipulate the magnetic soft robot, an understanding of the coupling between finite deformation and magnetic fields is required to model hard-magnetic soft materials. We consider the magnetoactive soft material as a homogenized continuum body with a constitutive law given by a Helmholtz free energy as a function of the Cauchy–Green tensor and magnetization in terms of the independent variables [45]. To facilitate physical interpretation and separation of the magneto-mechanical constitutive laws, as demonstrated in [46], [47], we divide the nominal Helmholtz free-energy density into an elastic part $\tilde{W}_{el}(\mathbf{F})$ as a function of the deformation gradient $\mathbf{F} \in \mathbb{R}^{3 \times 3}$, relating to both the reference and current configurations of the mSCR, and a magnetic part $\tilde{W}_{mag}(\mathbf{F}, \tilde{\mathbf{B}})$ as a function of the deformation gradient \mathbf{F} and the nominal magnetic flux density $\tilde{\mathbf{B}} \in \mathbb{R}^3$. This separation ensures that the elastic part can be linked to commonly used constitutive models for soft materials such as Neo-Hookean, Mooney–Rivlin, and Ogden. Considering that the mSCR integrates cables, the strain deformation does not justify the use of complex models such as Yeoh or Ogden. Moreover, as the Mooney–Rivlin model has a linear dependence on the two principal invariants (I_1, I_2), and the second invariant mainly governs shear deformation, we reduce the problem to its Neo-Hookean form, which is independent of the second invariant. The strain-energy density is then given by

$$W_{el} = C_1(I_1 J^{-2/3} - 3) + D_1(J - 1)^2$$

Where C_1 and D_1 are material constants which, by consistency with linear elasticity, can be expressed respectively as half the bulk and shear moduli, and J is the determinant of \mathbf{F} .

We then consider a locally uniform magnetic field $\mathbf{B}_{EPM} \in \mathbb{R}^3$ generated by the EPM, or electromagnetic coils (Fig. S3, S4), and a mSCR of length L and radius r , with a young modulus E and a uniform remanence \tilde{B}_r , so that the orthogonal magnetic torque at position x on the mSCR can be expressed as

$$\tau(x) = \mu_0^{-1} |\tilde{\mathbf{B}}_r| |\mathbf{B}_{EPM}| r^2 (L - x)$$

And the maximal deflection δ_{max} can then be derived as

$$\delta_{max} = \frac{4 |\tilde{\mathbf{B}}_r| |\mathbf{B}_{EPM}| L^3}{3 E \mu_0 r^2 \pi}$$

Where μ_0 is the magnetic permeability of free space ($4\pi \times 10^{-7}$ N.A $^{-2}$). The robotic end-effector was controlled in Cartesian space by means of an incremental algorithm. The magnetic interaction between the EPM and the mSCR is modelled using a magnetic dipole expansion and builds on previous work, with B_{EPM} related to the pose as follows:

$$\mathbf{B}_{EPM} = \frac{\mu_0 |\mathbf{m}|}{4\pi |\mathbf{p}|^3} (3\hat{\mathbf{p}}\hat{\mathbf{p}}^T - I_3)\hat{\mathbf{m}}$$

where $\mathbf{p} \in \mathbb{R}^3$ represents the position of the EPM, $\mathbf{m} \in \mathbb{R}^3$ is the magnetic dipole moment, and $|\cdot|$ denotes the Euclidean norm, with $\hat{\cdot} = \frac{\cdot}{|\cdot|}$. The pose of the EPM, for the desired field, derived from the optimization, is then given by:

$$\begin{aligned} |\mathbf{p}| &= \left(\frac{2\pi |\mathbf{B}_{EPM}|}{\mu_0 |\mathbf{m}|} \right)^{1/3} \\ \hat{\mathbf{m}} &= \frac{(3\hat{\mathbf{p}}\hat{\mathbf{p}}^T - I_3)^{-1}}{|3\hat{\mathbf{p}}\hat{\mathbf{p}}^T - I_3|} \hat{\mathbf{B}}_{EPM} \end{aligned}$$

At every time-step, the position variation ($\delta\mathbf{p}$) and heading increment ($\delta\hat{\mathbf{m}}$) with respect to the previous step are computed and sent to the low-level controller.

Autonomous insertion

Autonomous ERCP was enabled by an orientation estimation pipeline that couples a convolutional neural network detector (YOLOv8), trained to detect mSCR markers and the anatomical landmark (the papilla), with an algorithm that computes the geometric angle between these markers. The markers present on the mSCR (Fig. 5, 6) consist of 1-mm sections of soft heat-shrink tubing, positioned 10 mm apart. Each marker has a distinct color, allowing it to be distinguished from the others and from the environment.

Because labeled *in vivo* datasets are scarce, we assembled a training set from fresh *ex vivo* and carcass trials, as well as from a prior exploratory *in vivo* procedure, spanning four endoscope models and three illumination settings, and applied data augmentation. We then trained the model to identify classes corresponding to the different markers so that, for each frame, among all detections, the one with the highest confidence score for each class of interest was retained. On a held-out evaluation set, the detector achieved a precision of 0.81, a recall of 0.76, and an F1 score of 0.78.

For each saved bounding box, our algorithm then computes the centroid as the average of its four corner coordinates. Two vectors are constructed: one from the second mSCR marker to the papilla entry, and one from the first to the second mSCR marker. The angle between these two vectors represents the angular correction required to align the mSCR with the papilla.

The orientation error is mapped to a desired catheter deformation using our previously identified deformation-versus-field model. From the desired field, a magnetic torque command is derived, and the EPM pose is updated incrementally by a damped least-squares Cartesian controller.

For safety, the commanded orientation change was compared with the FBG shape reconstruction. The latter was streamed at 27 Hz to match the video frame rate, providing curvature and strain consistency checks.

Ultrasound Triggered Drug Release Shell design and fabrication

As the shell is a vibrationally driven system, that requires both deep-tissue penetration and spectral separation from imaging ultrasound, it was designed to resonate at 1 MHz.

Starting from a simple square pattern, we first performed mechanical-impedance analysis ($\zeta = F/u$) to select a set of geometric parameters (edge length, depth). We then ran finite-element modal analysis (ANSYS 2023, Ansys Inc., USA) to extract the resonant modes of the patterned tiles. This confirmed that a micro-pattern comprising interconnected PLA square tiles with 20 μm edge length and 5 μm depth, separated by 10 μm spacing, resonates near 1 MHz. A negative mold with the optimized geometry was printed on an ultra-high-resolution 3D printer (microArch® S140).

Because access to cytotoxic agents is restricted, povidone-iodine (PVP-I; $(\text{C}_6\text{H}_9\text{NO})_n \cdot (\text{I}_2)_m$) was used as a model payload for its enzyme reactivity in the pancreaticobiliary tract and tincture visibility on tissue. A gelatin (150 Bloom, Scientific Laboratory Supplies, UK) / PVP-I (Videne, Ecolab, MN, USA) / deionized cold-water pre-mix (mass ratio 1:0.5:5) was prepared by blooming for 30 s, then mixing at 60 °C and 800 rpm on a hot-plate magnetic stirrer (Heidolph MR-Hei Standard, Germany). The mixture was quenched at -18 °C to prevent sedimentation, milled, incorporated into a PLA matrix, and spin-coated (WS-650-23, Laurell) onto the printed mold to form a thin, drug-loaded shell. The film's thinness allowed conformal shaping over the mSCR, and it was bonded using a water-activated polyurethane adhesive (Gorilla Glue, USA).

Bench validation was performed in a water bath held at physiological temperature. To emulate acoustic attenuation/scattering and ensure consistent coupling, samples were isolated in 3D-printed tubes (Elastic 50A Resin V2, Formlabs, USA), a resin with a stable ultrasound response and a sound speed close to that of soft tissue [48]. Continuous imaging was simulated with a Philips L9-3 probe at 7.2 MHz on an iU22 system. At 20, 25, and 30 min, sonomechanical activation was applied using

a 1 MHz collimated transducer (5 cm^2) driven by an SP300 sonoporation system (SONIDEL) in unfocused mode. A 400 nm LED enabled visualization of release, compatible with narrow-band imaging at 415 nm on the Evis X1-CV1500 (Olympus, Japan). Drug diffusion was quantified by video tracking (Blackmagic Cinema Camera 6K, Blackmagic Design, Australia) using Python 3.12.

During the in vivo trial, once the catheter reached the desired location, the operator inflated the balloon to anchor the catheter in position, allowing the use of the ultrasound probe (Fig. 3E2). The ultrasound probe was positioned over the epigastric region, approximately 2 cm below the xiphoid process, initially in a transverse orientation (Fig. S2). The first clinical landmark was the superior mesenteric artery, visible in cross-section as an anechoic structure surrounded by an echogenic wall. Just anterior to this, the comma-shaped structure of the portal–splenic confluence was identified. Once this structure was located, the probe was rotated clockwise to an approximately 11 o’clock position, elongating the portal venous segment. By then carefully sweeping the probe back and forth, the bile duct could be visualized as it travelled towards its entrance in the gallbladder region. Once the catheter was identified within the duct (Fig. 2F), the operator used the insufflation trigger to anchor the catheter intraluminally and activated a second 1 MHz transducer to trigger drug delivery (Fig. 2E). Drug delivery was also demonstrated in different gastrointestinal environments (esophagus, stomach, and colon) to showcase versatility and robustness across a range of pH conditions (Fig. S6).

Buckling-aware design of a magneto-sensitive hyperelastic balloon

When deflated, the balloon should maintain continuous magnetization within the catheter, remaining compatible with previously reported shape-forming techniques and complex magnetization [10]. To ensure this property, a thick-walled cylinder is required (diameter-to-thickness ratio > 10). This allows the compressive hoop stress to be accurately estimated and reduces the risk of kinking, a localized form of buckling [49], while enabling shape-forming for navigation.

Once inflated, the relationship between pressure, force, and deformation can be expressed using the Yeoh strain-energy density function,

$$W = \sum_{i=1}^N C_i (\lambda_r^2 + \lambda_\theta^2 + \lambda_z^2 - 3)^i$$

where N is the polynomial order and C_i are the material constants. The Yeoh model was preferred over the Ogden model in this scenario due to the lack of a straightforward analytic model arising from irrational numbers in the material constants, leading to non-integrability of the force–pressure–deformation expression. For a third-order Yeoh model ($i = 3$), the analytical solutions for pressure and axial force were computed using Maple as functions of C_1 , C_2 , and C_3 , under the assumption of zero axial stretch, as:

$$\Delta p = \tilde{p}(\lambda_{in}, 1) - \tilde{p}(\lambda_{ex}, 1) \text{ and } f_{ex} = \tilde{f}(\lambda_{in}, 1) - \tilde{f}(\lambda_{ex}, 1)$$

For clarity, the full expressions are provided in the supplementary material.

A recurrent issue noted in the literature for soft balloons is buckling during inflation, often linked to the absence of a suitable model or to the use of strain-energy functions that exclude certain bifurcation features (Neo-Hookean, Mooney–Rivlin). In our case, the anchoring section is subjected to internal and external pressure, while potentially experiencing axial loading during gripper actuation; these phenomena had to be modeled to derive geometric parameters that avoid instability. Using the Ogden model [30], three types of bifurcations were analyzed: prismatic bifurcation leading to non-axial deformation; axisymmetric bifurcation leading to loss of cylindricity; and

asymmetric bifurcation leading to non-uniform expansion. The corresponding bifurcation criteria can be expressed, without loss of generality, as:

$$\begin{cases} \int_{\lambda_{r_{out}}}^{\lambda_{r_{in}}} \frac{\frac{\partial^2 \hat{W}}{\partial \lambda^2} \lambda d\lambda}{(\lambda^2 \lambda_z - 1) \left(\frac{\partial \hat{W}}{\partial \lambda} \right)^2} \\ \lambda_z > \frac{n\pi R_{out}}{\lambda_z^{3/2} L} \end{cases}$$

λ is equal to the ratio between the radius after (r) and before deformation (R) as r/R , $-_{in}$ and $-_{out}$ describe the radius to the inner wall and the outer wall respectively. λ_z is the axial extension ratio, which in our case is equal to 1 as axial deformation is considered negligible due to the presence of the cables, and L is the balloon height. W is the strain energy density function.

For the first criterion, under the assumption of incompressibility, the deformation should be described as:

$$r_{out}^2 = \sqrt{\lambda_z} (R_{out}^2 - R_{in}^2) + r_{in}^2$$

The set of values r_{in} , r_{out} can be selected following the boundary conditions described in [50], so as to satisfy both the prismatic and asymmetric bifurcation criteria simultaneously. The second criterion highlights, that for each value of λ_z , there is a maximum tube thickness beyond which axisymmetric bifurcations do not occur with increasing pressure. This value can be obtained by plotting λ_z against $\frac{n\pi R_{out}}{\lambda_z^{3/2} L}$ and the resulting curve provides a critical value of λ_z . Bifurcation into an axisymmetric mode in compression cannot occur for values of λ_z greater than this critical value.

When interconnecting two or more balloons, additional instability must be considered. For two interconnected balloons [51] (Fig. 3F, G), with radii R_a and R_b , and defining $\lambda_i = R_i/r_0$, the snap-through instability can drive fluid flow from the smaller-volume balloon to the larger one. Under the same internal pressure, the equilibrium can be written explicitly as:

$$\left(\frac{1}{\lambda_a} - \frac{1}{\lambda_a^2} \right) \left(1 + \frac{1}{K} \lambda_a^2 \right) = \left(\frac{1}{\lambda_b} - \frac{1}{\lambda_b^2} \right) \left(1 + \frac{1}{K} \lambda_b^2 \right)$$

where K is a material constant. The bifurcation branches off from the symmetric solution at the point $\lambda = \mu$ which corresponds to the maximum of the pressure–radius relation. Beyond this point, either both balloons proceed symmetrically downwards in pressure, or one balloon grows while the other falls back in pressure and radius. As pressure increases with the growing balloon radius up to a critical value p_{cr} , snap-through occurs and the balloon suddenly expands to a larger radius due to the highly non-linear elasticity of the rubber.

Compliant gripper

To model elastic deformation of the flexible element, we approximate it as a beam in which bending dominates over shear [52], [53]. Under the assumption of a pure end-load $f = [f_x \ f_y \ M]^T$ generating a variable tangent angle $\varphi(s)$ with the distance along the neutral axis $S \in [0, L]$, where L is the beam length, the curvature of the beam φ' can be integrated using a smooth curvature model. Previous research has shown that shifted Legendre polynomials are a good choice, allowing low-order but high-accuracy prediction of large deformation [54]:

$$\phi'(s, \alpha) = \frac{\alpha_0}{L} + \frac{\alpha_1}{L} \left(\frac{2s}{L} - 1 \right) + \frac{\alpha_2}{L} \left(\frac{6s^2}{L^2} - \frac{6s}{L} + 1 \right)$$

The coefficients $\alpha = [\alpha_0 \ \alpha_1 \ \alpha_2]^T$ serve as generalized coordinates that describe the flexure configuration. This generic formulation is applied to determine the deformation of the gripper under the pulling force required to close it, as well as to calculate the mSCR tip coordinates under the loading generated by gripper actuation. Material and geometric differences between the gripper and the mSCR arise when deriving the energy function under the same smooth-curvature basis (see supplementary material). We then established a simple system of equations linking the gripper actuation force to the resulting mSCR deformation. As the force required to actuate the gripper depends on geometric parameters, we ran an optimization over the gripper geometry to achieve the smallest acceptable mSCR deformation.

The final part of the gripper parametrization concerned the mechanical ultrasound drug delivery. To avoid matching the natural frequencies of the gripper beams with that of the drug coating (and to ensure structural integrity), we pre-twisted the beams. Pre-twisting increases stiffness and raises the natural frequency [54], [55], whose dimensionless expression can be calculated as:

$$\bar{w} = w \left(\frac{\rho A L^4}{\sqrt{EI_{xx}EI_{yy}}} \right)^{\frac{1}{2}}$$

Once designed, the grippers were then manufactured using an ultra-high resolution 3D printer (microArch® S140, Boston Micro Fabrication, MA, USA) using the HTL resin.

We validated that the actuation-force minimization did not alter the soft-body shape by driving the catheter with a single-axis coil and comparing mSCR deformations with the gripper unactuated versus actuated. We also validated the actuation-force model by connecting the actuation wire to a load cell (F/T Sensor Nano17 Titanium, ATI, MA, USA) and a linear translation stage (NRT150, Thorlabs, NJ, USA) (Fig. S7). By inverting this set-up, we characterized the gripping force. Tests were performed with and without balloon stabilization, demonstrating increased gripping force when using the balloon (Fig. 4D).

In vivo procedures

In vivo experiments were conducted on two Yorkshire–Landrace gilts weighing 33 kg and 35 kg under terminal general anesthesia at the Large Animal Experimental Facility, University of Leeds. All procedures complied with the UK Animal (Scientific Procedures) Act 1986 under Home Office license PPL PP3093153 and followed NC3Rs and ARRIVE guidelines.

In line with the protocol described in [56], a high-energy liquid diet was used to produce a clean gastrointestinal tract without causing detectable physiological or behavioral abnormalities. Both gilts were placed in the supine position. The endoscope was advanced 90–100 cm through the upper gastrointestinal tract to the major papilla and into the pancreatic duct, with insufflation and suction or irrigation used as required.

Species-specific anatomical differences, including the more distal minor papilla, were accounted for during procedures. However, despite this variation, pigs have long been employed as models for human gastrointestinal research [57], [58], [59].

Biological safety assessment

To be as close as possible to a clinical scenario, prototypes used during the in-vivo trial were processed according to the ISO 17664 (cleaning, sterilization and storage) and to the ISO 10993 (cytotoxicity evaluation) [42].

On the morning before the trials, catheters were cleaned in a 500 ml hospital-grade disinfectant solution (Rely+On, Virkon) then rinsed with water. They were then placed in sterilization pouches and autoclaved at 121 °C for half an hour followed by half an hour drying. Catheters were kept in the pouches until use and disposed afterward following infectious healthcare waste protocol.

To assess the cytotoxicity of the doped silicon (DS30) with metals-metalloids (NdFeB) microparticles used to fabricate the mSCR, the viability of human fetal foreskin fibroblast 2 (HFFF2) in direct contact with the composite materials was studied over 24 hours. The HFFF2 fibroblasts were seeded in culture medium then exposed to different combinations of DS and NdFeB (Supp file) and compared to positive control (cells only) and negative control (cells+NdFeB), to elicit a cytotoxic response. Cell viability was quantified using the CellTiter-Glo® 2D Cell Viability Assay (Promega), which measures intracellular ATP as an indicator of metabolically active cells. The results showed that there was no significant difference in the metabolic activity of the cells between the different conditions for a 24-hour exposure time.

Acknowledgments: We thank E. Murphy, J. Bilton, S. Wilson and A. Alexander for their support.

Fundings:

Advanced Research and Invention Agency (ARIA)

Engineering and Physical Sciences Research Council (EPSRC) grant EP/V009818/1

European Research Council (ERC) through the European Union's Horizon 2020 Research and Innovation Programme under Grant 818045

J. Chandler was supported by the Leverhulme Trust and the Royal Academy of Engineering under a RAEEng/Leverhulme Trust Research Fellowship (LTRF-2425-21-154)

Any opinions, findings and conclusions, or recommendations expressed in this article are those of the authors and do not necessarily reflect the views of the ARIA, the EPSRC, or the ERC.

Competing interests: Authors declare that they have no competing interests.

References

- [1] M. Cianchetti, C. Laschi, A. Menciassi, and P. Dario, 'Biomedical applications of soft robotics', *Nat. Rev. Mater.*, vol. 3, no. 6, pp. 143–153, Jun. 2018, doi: 10.1038/s41578-018-0022-y.
- [2] O. Yasa *et al.*, 'An Overview of Soft Robotics', *Annu. Rev. Control Robot. Auton. Syst.*, vol. 6, no. 1, pp. 1–29, May 2023, doi: 10.1146/annurev-control-062322-100607.
- [3] C. Della Santina, C. Duriez, and D. Rus, 'Model-Based Control of Soft Robots: A Survey of the State of the Art and Open Challenges', *IEEE Control Syst. Mag.*, vol. 43, no. 3, pp. 30–65, Jun. 2023, doi: 10.1109/MCS.2023.3253419.
- [4] S. J. Woodman, D. S. Shah, M. Landesberg, A. Agrawala, and R. Kramer-Bottiglio, 'Stretchable Arduinos embedded in soft robots', *Sci. Robot.*, vol. 9, no. 94, p. eadn6844, Sep. 2024, doi: 10.1126/scirobotics.adn6844.
- [5] E. Milana, C. D. Santina, B. Gorissen, and P. Rothemund, 'Physical control: A new avenue to achieve intelligence in soft robotics', *Sci. Robot.*, vol. 10, no. 102, p. eadw7660, May 2025, doi: 10.1126/scirobotics.adw7660.
- [6] M. Russo *et al.*, 'Continuum Robots: An Overview', *Adv. Intell. Syst.*, vol. 5, no. 5, 2023.
- [7] R. Dreyfus *et al.*, 'Dexterous helical magnetic robot for improved endovascular access', *Sci. Robot.*, vol. 9, no. 87, p. eadh0298, Feb. 2024, doi: 10.1126/scirobotics.adh0298.
- [8] Y. Kim *et al.*, 'Telerobotic neurovascular interventions with magnetic manipulation', *Sci. Robot.*, vol. 7, no. 65, p. eabg9907, Apr. 2022, doi: 10.1126/scirobotics.abg9907.
- [9] Y. Kim, H. Yuk, R. Zhao, S. A. Chester, and X. Zhao, 'Printing ferromagnetic domains for untethered fast-transforming soft materials', *Nature*, vol. 558, no. 7709, pp. 274–279, Jun. 2018, doi: 10.1038/s41586-018-0185-0.
- [10] P. Lloyd, G. Pittiglio, J. H. Chandler, and P. Valdastri, 'Optimal Design of Soft Continuum Magnetic Robots under Follow-the-leader Shape Forming Actuation', in *2020 International Symposium on Medical Robotics (ISMR)*, Nov. 2020, pp. 111–117. doi: 10.1109/ISMR48331.2020.9312943.
- [11] Y. Dong *et al.*, 'Untethered small-scale magnetic soft robot with programmable magnetization and integrated multifunctional modules', *Sci. Adv.*, vol. 8, no. 25, p. eabn8932, Jun. 2022, doi: 10.1126/sciadv.abn8932.
- [12] Y. Cao *et al.*, 'Magnetic Continuum Robot With Modular Axial Magnetization: Design, Modeling, Optimization, and Control', *IEEE Trans. Robot.*, vol. 41, pp. 1513–1532, 2025, doi: 10.1109/TRO.2025.3526077.

[13] L. Pancaldi, E. Özelti, M. A. Gadiri, J. Raub, P. J. Mosimann, and M. S. Sakar, ‘Flow-driven magnetic microcatheter for superselective arterial embolization’, *Sci. Robot.*, vol. 10, no. 107, p. eadu4003, Oct. 2025, doi: 10.1126/scirobotics.adu4003.

[14] G. Pittiglio *et al.*, ‘Personalized magnetic tentacles for targeted photothermal cancer therapy in peripheral lungs’, *Commun. Eng.*, vol. 2, no. 1, pp. 1–13, Jul. 2023.

[15] Z. Chen, B. Rivkin, D. Castellanos-Robles, I. Soldatov, L. Beyer, and M. Medina-Sánchez, ‘Rapid Fabrication of Self-Propelled and Steerable Magnetic Microcatheters for Precision Medicine’, *Adv. Mater.*, vol. n/a, no. n/a, p. e06591, doi: 10.1002/adma.202506591.

[16] J. Yang *et al.*, ‘Magnetically actuated multimodal bioelectronic catheter for minimally invasive surgery and sensing’, *Nat. Mater.*, Sep. 2025, doi: 10.1038/s41563-025-02340-5.

[17] C. Zhou *et al.*, ‘Ferromagnetic soft catheter robots for minimally invasive bioprinting’, *Nat. Commun.*, vol. 12, no. 1, p. 5072, Aug. 2021, doi: 10.1038/s41467-021-25386-w.

[18] S. Yang, J. Shen, J. He, Z. Xia, Y. Zhang, and B. Wang, ‘Magnetic slippery microcatheter with artificial cilia for low-friction interventions’, *Sci. Adv.*, vol. 11, no. 42, p. eadw9926, Oct. 2025, doi: 10.1126/sciadv.adw9926.

[19] F. C. Landers *et al.*, ‘Clinically ready magnetic microrobots for targeted therapies’, *Science*, vol. 390, no. 6774, pp. 710–715, Nov. 2025, doi: 10.1126/science.adx1708.

[20] P. D. Leiphrakpam, S. Chowdhury, M. Zhang, V. Bajaj, M. Dhir, and C. Are, ‘Trends in the Global Incidence of Pancreatic Cancer and a Brief Review of its Histologic and Molecular Subtypes’, *J. Gastrointest. Cancer*, vol. 56, no. 1, p. 71, Dec. 2025, doi: 10.1007/s12029-025-01183-2.

[21] A. S. Köksal, A. T. Eminler, and E. Parlak, ‘Biliary endoscopic sphincterotomy: Techniques and complications’, *World J. Clin. Cases*, vol. 6, no. 16, pp. 1073–1086, Dec. 2018, doi: 10.12998/wjcc.v6.i16.1073.

[22] I. Malenica, M. Donadon, and A. Lleo, ‘Molecular and Immunological Characterization of Biliary Tract Cancers: A Paradigm Shift Towards a Personalized Medicine’, *Cancers*, vol. 12, no. 8, p. 2190, Aug. 2020, doi: 10.3390/cancers12082190.

[23] B. Calmé *et al.*, ‘Hybrid Tendon-Actuated and Soft Magnetic Robotic Platform for Pancreatic Applications’, *IEEE Robot. Autom. Lett.*, vol. 10, no. 2, pp. 1784–1791, Feb. 2025, doi: 10.1109/LRA.2024.3524889.

[24] Q. Boehler, S. Gervasoni, S. L. Charreyron, C. Chautems, and B. J. Nelson, ‘On the Workspace of Electromagnetic Navigation Systems’, *IEEE Trans. Robot.*, vol. 39, no. 1, pp. 791–807, Feb. 2023, doi: 10.1109/TRO.2022.3197107.

[25] S. C. T. Moorcroft *et al.*, ‘Ultrasound-Triggered Release of Anticancer Nanoparticles from Electrospun Fabrics Integrated with Soft Robotic Tentacles’, *Adv. NanoBiomed Res.*, p. 2500052, Oct. 2025, doi: 10.1002/anbr.202500052.

[26] B. Gorissen, D. Reynaerts, S. Konishi, K. Yoshida, J.-W. Kim, and M. De Volder, ‘Elastic Inflatable Actuators for Soft Robotic Applications’, *Adv. Mater.*, vol. 29, no. 43, p. 1604977, 2017, doi: 10.1002/adma.201604977.

[27] D. Van Lewen, T. Janke, H. Lee, R. Austin, E. Billatos, and S. Russo, ‘A Millimeter-Scale Soft Robot for Tissue Biopsy Procedures’, *Adv. Intell. Syst.*, vol. 5, no. 5, p. 2200326, May 2023, doi: 10.1002/aisy.202200326.

[28] V. Del Bono *et al.*, ‘A soft robotic “Add-on” for colonoscopy: increasing safety and comfort through force monitoring’, *Npj Robot.*, vol. 3, no. 1, p. 15, Jun. 2025, doi: 10.1038/s44182-025-00028-1.

[29] L. Manfredi, E. Capoccia, G. Ciuti, and A. Cuschieri, ‘A Soft Pneumatic Inchworm Double balloon (SPID) for colonoscopy’, *Sci. Rep.*, vol. 9, no. 1, Jul. 2019.

[30] D. M. Haughton and R. W. Ogden, ‘Bifurcation of inflated circular cylinders of elastic material under axial loading—II. Exact theory for thick-walled tubes’, *J. Mech. Phys. Solids*, vol. 27, no. 5–6, pp. 489–512, Dec. 1979, doi: 10.1016/0022-5096(79)90027-9.

[31] F. Ullrich, K. S. Dheman, S. Schuerle, and B. J. Nelson, ‘Magnetically actuated and guided milli-gripper for medical applications’, in *2015 IEEE International Conference on Robotics and Automation (ICRA)*, May 2015, pp. 1751–1756. doi: 10.1109/ICRA.2015.7139424.

[32] J. Dearden, C. Grames, B. D. Jensen, S. P. Magleby, and L. L. Howell, ‘Inverted L-Arm Gripper Compliant Mechanism’, *J. Med. Devices*, vol. 11, Jun. 2017.

[33] J. W. Byun *et al.*, ‘Usefulness of Forward-Viewing Endoscope for Endoscopic Retrograde Cholangiopancreatography in Patients with Billroth II Gastrectomy’, *Clin. Endosc.*, vol. 45, no. 4, pp. 397–403, Nov. 2012, doi: 10.5946/ce.2012.45.4.397.

[34] H. S. Khara, S. Parvataneni, S. Park, J. Choi, T. H. Kothari, and S. T. Kothari, ‘Review of ERCP Techniques in Roux-en-Y Gastric Bypass Patients: Highlight on the Novel EUS-Directed Transgastric ERCP (EGDE) Technique’, *Curr. Gastroenterol. Rep.*, vol. 23, no. 7, p. 10, Jul. 2021, doi: 10.1007/s11894-021-00808-3.

[35] M. S. Kim, Y. H. Kim, Y. Choi, and K. Y. Lee, ‘Biohybrid actuators in robotics: recent trends and future perspectives of skeletal and cardiac muscle integration’, *Npj Robot.*, vol. 3, no. 1, p. 37, Nov. 2025, doi: 10.1038/s44182-025-00049-w.

[36] L. Ricotti *et al.*, ‘Biohybrid actuators for robotics: A review of devices actuated by living cells’, *Sci. Robot.*, vol. 2, no. 12, p. eaaq0495, Nov. 2017, doi: 10.1126/scirobotics.eaaq0495.

[37] C. Wang *et al.*, ‘Bioinspired liquid gating membrane-based catheter with anticoagulation and positionally drug release properties’, *Sci. Adv.*, vol. 6, no. 36, p. eabb4700, Sep. 2020, doi: 10.1126/sciadv.abb4700.

[38] H. Torlakcik *et al.*, ‘Magnetically Guided Microcatheter for Targeted Injection of Magnetic Particle Swarms’, *Adv. Sci.*, vol. 11, no. 38, p. 2404061, Oct. 2024, doi: 10.1002/advs.202404061.

[39] A. Z. Taddese, P. R. Slawinski, M. Pirotta, E. De Momi, K. L. Obstein, and P. Valdastri, ‘Enhanced real-time pose estimation for closed-loop robotic manipulation of magnetically actuated capsule endoscopes’, *Int. J. Robot. Res.*, vol. 37, no. 8, pp. 890–911, Jul. 2018, doi: 10.1177/0278364918779132.

[40] D. Von Arx, B. J. Nelson, and Q. Boehler, ‘Orthogonal Pulse-Width-Modulation for Combined Electromagnetic Actuation and Localization’, *IEEE Robot. Autom. Lett.*, vol. 10, no. 6, pp. 6424–6431, Jun. 2025, doi: 10.1109/LRA.2025.3568324.

[41] M. Mattille *et al.*, ‘Advancing Minimally Invasive Precision Surgery in Open Cavities with Robotic Flexible Endoscopy’, Nov. 18, 2025, *arXiv*: arXiv:2511.14458. doi: 10.48550/arXiv.2511.14458.

[42] C. Rumbo *et al.*, ‘In vitro safety evaluation of rare earth-lean alloys for permanent magnets manufacturing’, *Sci. Rep.*, vol. 11, no. 1, p. 12633, Jun. 2021, doi: 10.1038/s41598-021-91890-0.

[43] V. Chandrasekhara *et al.*, ‘Adverse events associated with ERCP’, *Gastrointest. Endosc.*, vol. 85, no. 1, pp. 32–47, Jan. 2017, doi: 10.1016/j.gie.2016.06.051.

[44] K. Bishay *et al.*, ‘Adverse Events Associated With Endoscopic Retrograde Cholangiopancreatography: Systematic Review and Meta-Analysis’, *Gastroenterology*, vol. 168, no. 3, pp. 568–586, Mar. 2025, doi: 10.1053/j.gastro.2024.10.033.

[45] A. Dorfmann and R. W. Ogden, ‘Nonlinear magnetoelastic deformations of elastomers’, *Acta Mech.*, vol. 167, no. 1–2, pp. 13–28, Jan. 2004, doi: 10.1007/s00707-003-0061-2.

[46] L. Dorfmann and R. W. Ogden, ‘Hard-magnetic soft magnetoelastic materials: Energy considerations’, *Int. J. Solids Struct.*, vol. 294, p. 112789, May 2024, doi: 10.1016/j.ijsolstr.2024.112789.

[47] R. Zhao, Y. Kim, S. A. Chester, P. Sharma, and X. Zhao, ‘Mechanics of hard-magnetic soft materials’, *J. Mech. Phys. Solids*, vol. 124, pp. 244–263, Mar. 2019, doi: 10.1016/j.jmps.2018.10.008.

[48] M. Mencarelli, L. Puggelli, A. Virga, R. Furferi, and Y. Volpe, ‘Acoustic velocity and stability of tissue-mimicking echogenic materials for ultrasound training phantoms’, *J. Mater. Sci.*, vol. 59, no. 15, pp. 6509–6524, Apr. 2024, doi: 10.1007/s10853-024-09610-8.

[49] N. J. Hoff, ‘Buckling of Thin Cylindrical Shell Under Hoop Stresses Varying in Axial Direction’, *J. Appl. Mech.*, vol. 24, no. 3, pp. 405–412, Sep. 1957, doi: 10.1115/1.4011554.

[50] A. Ertepınar, ‘Stability and vibrations of thick-walled tubes subjected to finite twist and external pressure’, *Int. J. Solids Struct.*, vol. 14, no. 9, pp. 715–722, 1978, doi: 10.1016/0020-7683(78)90030-6.

[51] I. Müller and P. Strehlow, Eds., *Rubber and Rubber Balloons: Paradigms of Thermodynamics*, vol. 637. in Lecture Notes in Physics, vol. 637. Berlin, Heidelberg: Springer Berlin Heidelberg, 2004. doi: 10.1007/b93853.

[52] V. K. Venkiteswaran and H.-J. Su, ‘A Versatile 3R Pseudo-Rigid-Body Model for Initially Curved and Straight Compliant Beams of Uniform Cross Section’, *J. Mech. Des.*, vol. 140, no. 9, p. 092305, Sep. 2018, doi: 10.1115/1.4040628.

[53] L. U. Odhner and A. M. Dollar, ‘The Smooth Curvature Model: An Efficient Representation of Euler–Bernoulli Flexures as Robot Joints’, *IEEE Trans. Robot.*, vol. 28, no. 4, pp. 761–772, Aug. 2012, doi: 10.1109/TRO.2012.2193232.

[54] J. R. Banerjee and H. Su, ‘Development of a dynamic stiffness matrix for free vibration analysis of spinning beams’, *Comput. Struct.*, vol. 82, no. 23–26, pp. 2189–2197, Sep. 2004, doi: 10.1016/j.compstruc.2004.03.058.

[55] W.-R. Chen, ‘On the vibration and stability of spinning axially loaded pre-twisted Timoshenko beams’, *Finite Elem. Anal. Des.*, vol. 46, no. 11, pp. 1037–1047, Nov. 2010, doi: 10.1016/j.finel.2010.07.020.

[56] R. Gregson, S. Greenhalgh, B. Cox, S. Cochrane, and R. E. Clutton, ‘Feeding management before gastrointestinal studies in pigs’, *Lab. Anim.*, vol. 55, no. 2, pp. 177–180, Apr. 2021, doi: 10.1177/0023677220960509.

[57] M. J. Truty and R. L. Smoot, ‘Animal Models in Pancreatic Surgery: A Plea for Pork’, *Pancreatology*, vol. 8, no. 6, pp. 546–550, Oct. 2008, doi: 10.1159/000160214.

[58] G. M. Ferreira *et al.*, ‘Anatomic and Surgical Aspects of Total Pancreatectomy in Swine’, *Transplant. Proc.*, vol. 56, no. 5, pp. 1134–1137, Jun. 2024, doi: 10.1016/j.transproceed.2024.04.020.

[59] D. Ligresti *et al.*, ‘EUS anatomy of the pancreaticobiliary system in a swine model: The WISE experience’, *Endosc. Ultrasound*, vol. 8, no. 4, p. 249, 2019, doi: 10.4103/eus.eus_10_19.

Supplementary Materials

Modeling of a thick cylindrical anchoring balloon

To model the balloon, we first define a reference (undeformed) configuration in which each material point is described by the coordinates (R, Θ, Z) , and a deformed configuration described by (r, θ, z) . In this setting, torsional effects are neglected; thus, under an internal pressure p_{in} , an external pressure p_{ex} , and an external axial force f_{ex} , the magnetic balloon undergoes radial (R) and axial (Z) deformation. Therefore, in cylindrical basis, the deformation gradient \mathbf{F} is given by:

$$\mathbf{F} = \begin{bmatrix} \frac{\partial r}{\partial R} & 0 & \frac{\partial r}{\partial Z} \\ 0 & \frac{r}{R} & 0 \\ 0 & 0 & \frac{\partial z}{\partial Z} \end{bmatrix}$$

Since the cylinder is closed at both ends, the radial deformation is not uniform along its longitudinal axis. The deformation increases progressively from each end and reaches a maximum; this maximum then remains constant over a central portion of the cylinder of length δZ . Therefore, the deformed radial coordinate can be written as:

$$r = f(R, Z), \frac{\partial f}{\partial Z} = 0 \forall Z \in \delta Z$$

For large deformations, we restrict attention to the diagonal terms of the matrix. Moreover, because the cables and fibres prevent axial extension, we take the axial deformation to be zero. The principal stretches are then:

$$\lambda_r = \frac{\partial f}{\partial R}, \lambda_\theta = \frac{r}{R}, \lambda_z = 1$$

Moreover, we assume an isochoric deformation, implying that volume is conserved throughout the deformation. For instance, the volume enclosed between the inner radius R_{in} and R in the reference configuration remains unchanged after deformation. This leads to the following relations:

$$R = \sqrt{r^2 - r_{in}^2 + R_{in}^2}$$

$$\lambda_\theta = \sqrt{\frac{r^2}{r^2 - r_{in}^2 + R_{in}^2}}$$

This allows us to express the relationship between Δp and λ_θ and in terms of strain energy function

$$\Delta p = \int_{\lambda_{ex}}^{\lambda_{in}} (\lambda_\theta^2 - 1)^{-1} \frac{\partial W}{\partial \lambda_\theta} d\lambda_\theta$$

where $\lambda_{in} = \frac{r_{in}}{R_{in}}$ and respectively for λ_{ex} .

We now solve the axial force equilibrium resulting from the gripper actuation

$$f_{ex} = f_{in} - P_{in} \pi r_{in}^2$$

Where P_{in} is the internal pressure, and f_{in} is the internal force generated at the cylinder cross-section; it can be expressed as a function of λ_θ

$$f_{in} = 2\pi \int_{\lambda_{ex}}^{\lambda_{in}} \sigma_z \Big|_{\lambda_z=1} \frac{r^2}{\lambda_\theta(\lambda_\theta^2 - 1)} d\lambda_\theta$$

Here, σ_z is one of the principal Cauchy stresses, expressed in terms of the strain energy function $W(\lambda_r, \lambda_\theta, \lambda_z)$

$$\sigma_i = -p_{in} + \lambda_i \frac{\partial W}{\partial \lambda_i}, \forall i = r, \theta, z$$

Applying Cauchy's first law of motion, the divergence of the stress tensor vanishes. Together with the volume-conservation assumption, this allows σ_z to be expressed as:

$$\sigma_z \Big|_{\lambda_z=1} = -p_{ex} + \frac{\partial \widehat{W}}{\partial \lambda_z} \Big|_{\lambda_z=1} - \int_{\lambda_{ex}}^{\lambda_\theta} \frac{\frac{\partial \widehat{W}}{\partial \lambda_\theta} \Big|_{\lambda_z=1}}{\lambda_\theta^2 - 1} d\lambda_\theta.$$

Then, substituting this into the expression for f_{in} and applying integration by parts, we obtain the following expression for f_{ex}

$$f_{ex} = \pi R_{in}^2 (\lambda_{in}^2 - 1) \int_{\lambda_{ex}}^{\lambda_{in}} \frac{2 \frac{\partial \widehat{W}}{\partial \lambda_z} \Big|_{\lambda_z=1} - \lambda_\theta \frac{\partial \widehat{W}}{\partial \lambda_\theta} \Big|_{\lambda_z=1}}{(\lambda_\theta^2 - 1)^2} \lambda_\theta d\lambda_\theta - p_{ex} \pi \lambda_{ex}^2 R_{ex}^2.$$

For the reasons mentioned above, we choose the Yeoh strain energy density function

$$W = \sum_{i=1}^N C_i (\lambda_r^2 + \lambda_\theta^2 + \lambda_z^2 - 3)^i$$

where N is the polynomial order and C_i are the material constants. For a third-order Yeoh model ($N = 3$), the analytical solutions for the pressure and axial force are computed in Maple as functions of C_1 , C_2 , and C_3 . They are given, respectively, by:

$$\Delta p = \tilde{p}(\lambda_{in}, 1) - \tilde{p}(\lambda_{ex}, 1)$$

$$f_{ex} = \tilde{f}(\lambda_{in}, 1) - \tilde{f}(\lambda_{ex}, 1)$$

Where

$$\tilde{p}(\lambda_\theta, 1) = \frac{-C_1 + 2C_2 - 10.5C_3 - 6C_3\lambda_\theta^2 - C_3\lambda_\theta^{-2}}{\lambda_\theta^2}$$

$$+ 2C_2\lambda_\theta^2 - 15C_3\lambda_\theta^2 - 1.5C_3\lambda_\theta^4 + \frac{6C_3\lambda_\theta^4 + 15C_3 - 2C_2}{\lambda_\theta^2} + \ln \lambda_\theta (2C_1 - 4C_2 + 12C_3)$$

And

$$f(\lambda_\theta, 1) = \pi(\lambda_{in}^2 - 1)(-6C_1 \ln(\lambda_\theta) - 2C_2\lambda_\theta^2 + 8C_2 \ln(\lambda_\theta) + \frac{16C_2}{\lambda_\theta^2} - \frac{2C_2}{\lambda_\theta^4}$$

$$- \frac{3}{2}C_3\lambda_\theta^4 + 12C_3\lambda_\theta^2 + 24C_3 \ln^2(\lambda_\theta^2 - 1) - 60C_3 \ln(\lambda_\theta^2 - 1) - \frac{30C_3}{\lambda_\theta^2} + \frac{39C_3}{2\lambda_\theta^4})$$

Dataset for the AI based detection model

To train and validate the model, we used 3,200 endoscopic images collected during various phantom, ex vivo, and cadaver trials to fine-tune the base YOLOv8 model. As one of the strengths of the mSCR is its platform versatility, five different endoscopes (Table S1) were used, resulting in images with two different resolutions (720×480 and 1920×1080) and three different brightness levels.

We created the dataset by manually annotating one third of the images with bounding polygons using Roboflow. A validation check was performed to ensure correct labeling of all images. The dataset was then partitioned into training, validation, and test sets with proportions (number of images) of 70% (2,240), 20% (640), and 10% (320), respectively.

Furthermore, to improve robustness, we generated augmented versions of each original training image using (i) horizontal and vertical flips with 50% probability, (ii) exposure adjustments between -9% and +9%, (iii) Gaussian blurring between 0 and 0.25 pixels, (iv) hue shifts between -25 and +25, and (v) cropping with up to 23% zoom. As a result, the number of images in the training set was quintupled to 11,200.

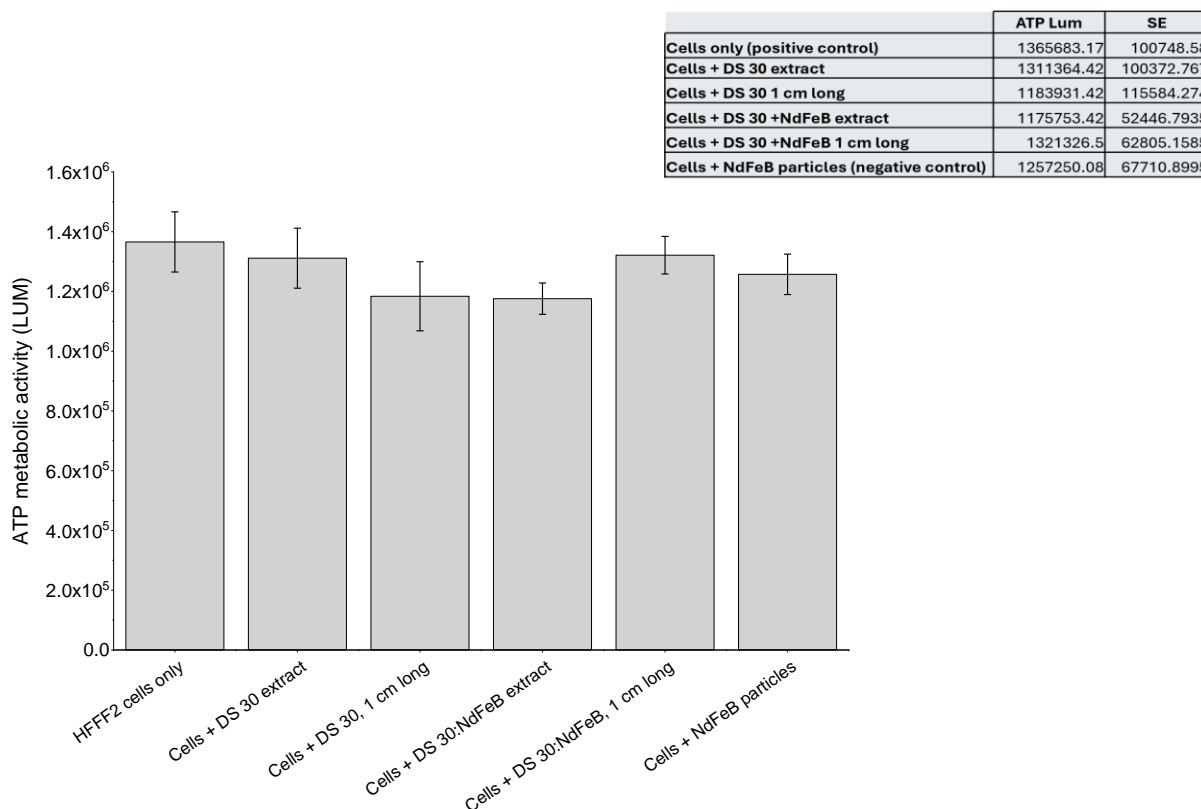
Biocompatibility analysis

To assess the biological response to the DS 30 and DS 30+NdFeB fibers, both fibers DS fibers were first autoclaved at 121 °C for approximately an hour. Under sterile conditions, they were then subjected to an extract preparation process to prepare conditioned media for cell culture. The conditioned media were prepared by incubating 10 mm segments of autoclaved DS 30 or DS 30+NdFeB fibers in 100 mL of Dulbecco's Modified Eagle Medium (DMEM; Thermo Fisher Scientific) supplemented with 10% foetal bovine serum (FBS; Sigma-Aldrich), 1% Penicillin-Streptomycin (P/S; Sigma-Aldrich), and 1% GlutaMAX (Thermo Fisher Scientific) in 75 cm² culture flasks at 37 °C for 48 hours with oscillation. As a negative control, NdFeB particles were diluted 1:10 in DMEM/10% FBS medium and incubated under identical conditions.

Human foetal foreskin fibroblast 2 (HFFF2) cells, provided by Dr Nicola Ingram (Molecular and Nanoscale Physics Research Group, School of Physics and Astronomy), were cultured in DMEM/10% FBS medium. Cells were seeded at a density of 5×10^4 cells per well in 24-well plates and maintained at 37 °C in a humidified (95-99%) incubator with 5% CO₂ until confluent.

Once confluent and with conditioned media prepared, the culture medium in each well was aspirated and replaced with 500 μ L of DS 30 conditioned medium, DMEM/10% FBS culture medium with 10 mm autoclaved DS 30 fiber, DS 30+NdFeB conditioned medium, DMEM/10% FBS culture medium with 10 mm autoclaved DS 30+NdFeB fiber, and DMEM/10% FBS culture medium with the prepared NdFeB particles at a dilution of 1:10. Cells were incubated for 24 h under standard cell culture conditions (37 °C, 5% CO₂, 95–99% humidity), and videos were acquired with IncuCyte® S3 Live-Cell Analysis System to observe cellular behavior under the different conditions.

Cell viability was quantified using the CellTiter-Glo® 2D Cell Viability Assay (Promega), which measures intracellular ATP as an indicator of metabolically active cells. A 1:1 volume of CellTiter-Glo reagent was added to each well, and the plates were placed on an orbital shaker for 2 min to induce cell lysis. Lysates were then transferred to opaque 96-well plates and incubated at room temperature for 10 min to stabilize the luminescent signal. Luminescence was measured using a Tecan Spark Microplate Reader (Low End, MIC9412).



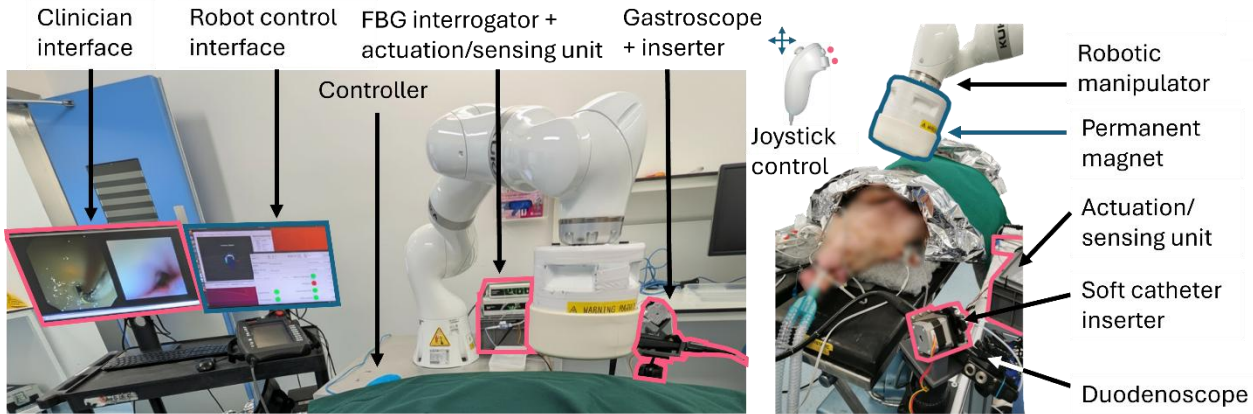


Figure S1: **In vivo experimental setup** (Left) Position of the robotic manipulator on the side of the pig, with the control screens and endoscope placement. In vivo view from the endoscope alongside the view from the mSCR. (Right) Joystick control for navigation of the robotic manipulator and the mSCR, with the endoscope fixed to the robotic cart and the actuation unit positioned adjacent to it.

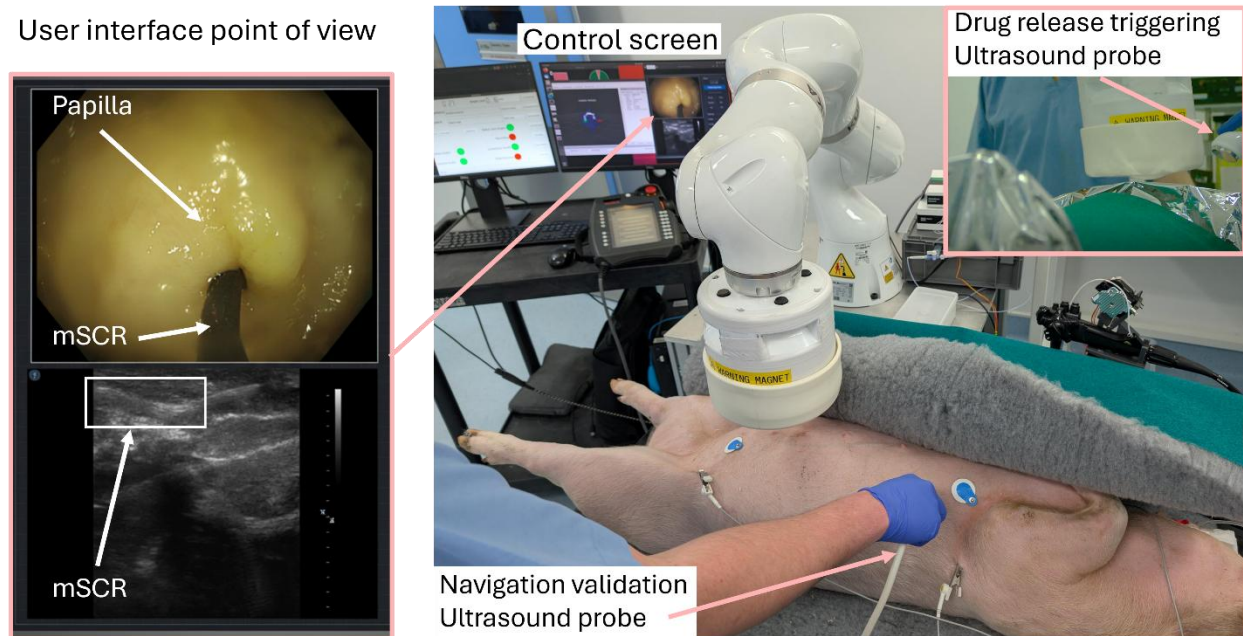


Figure S2: **In vivo experimental setup for drug release** (Left) In vivo endoscopic view alongside ultrasound feedback displayed on the user interface. (Right) Verification of the mSCR position within the pancreatic duct, followed by activation of the drug-release mechanism using the secondary probe (top right detail).

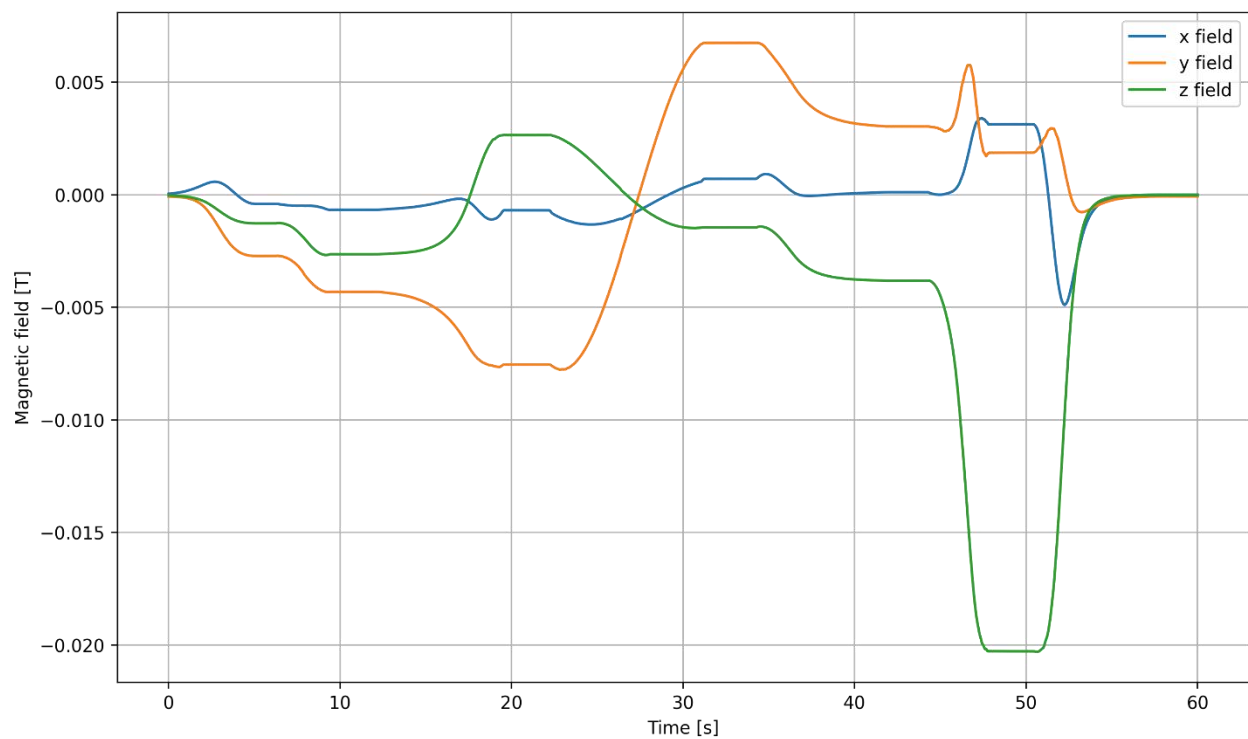
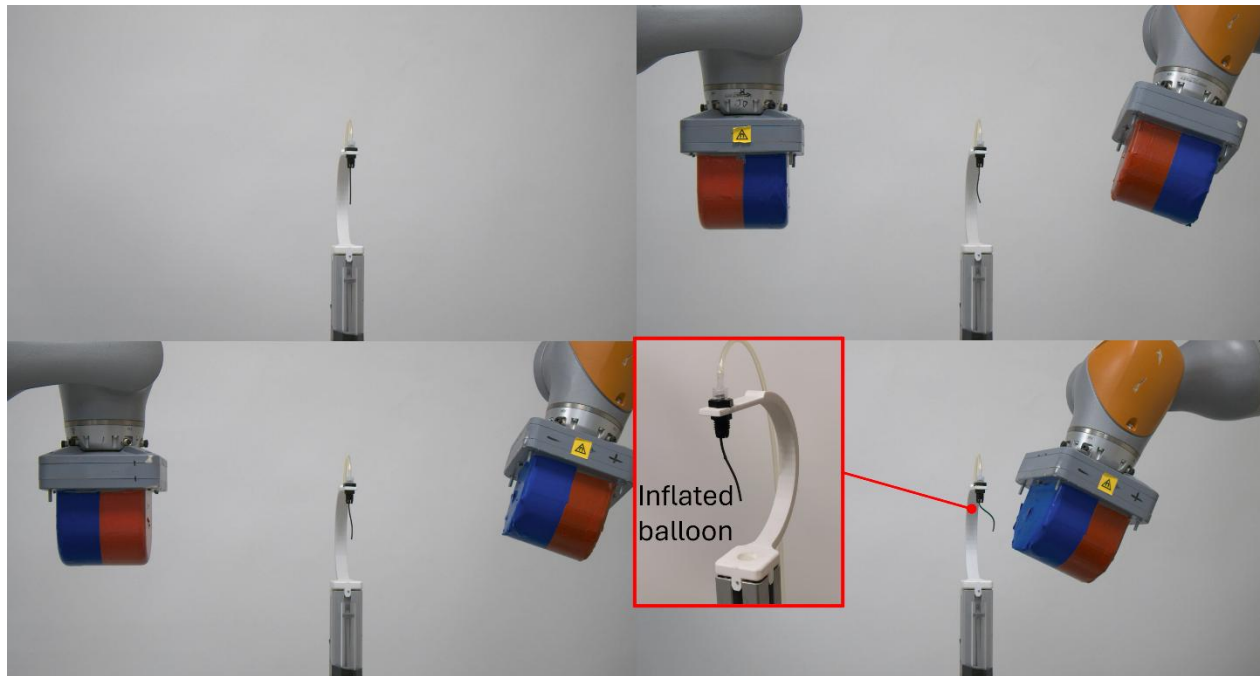


Figure S3 Demonstration of the conservation of the ability to perform shape forming using the dual permanent magnet platform [1], while integrating the magnetic balloon

[1] G. Pittiglio et al., 'Personalized magnetic tentacles for targeted photothermal cancer therapy in peripheral lungs', *Commun. Eng.*, vol. 2, no. 1, pp. 1–13, Jul. 2023.

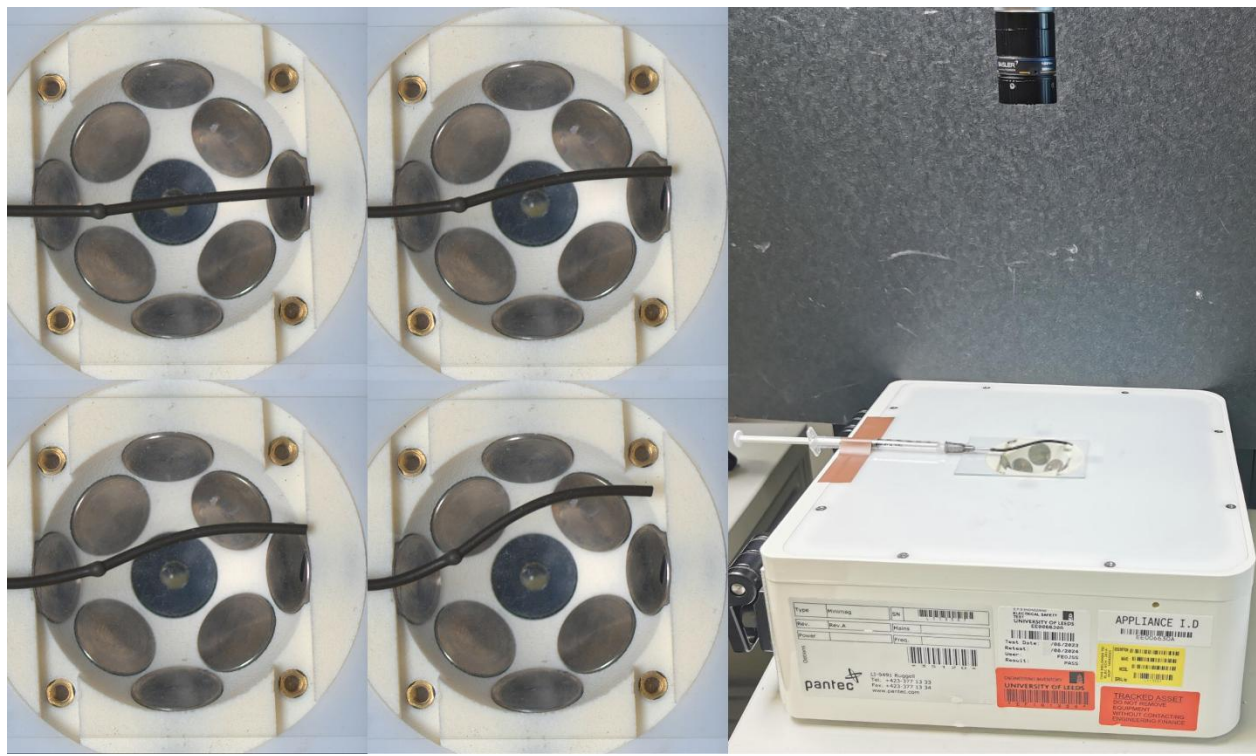
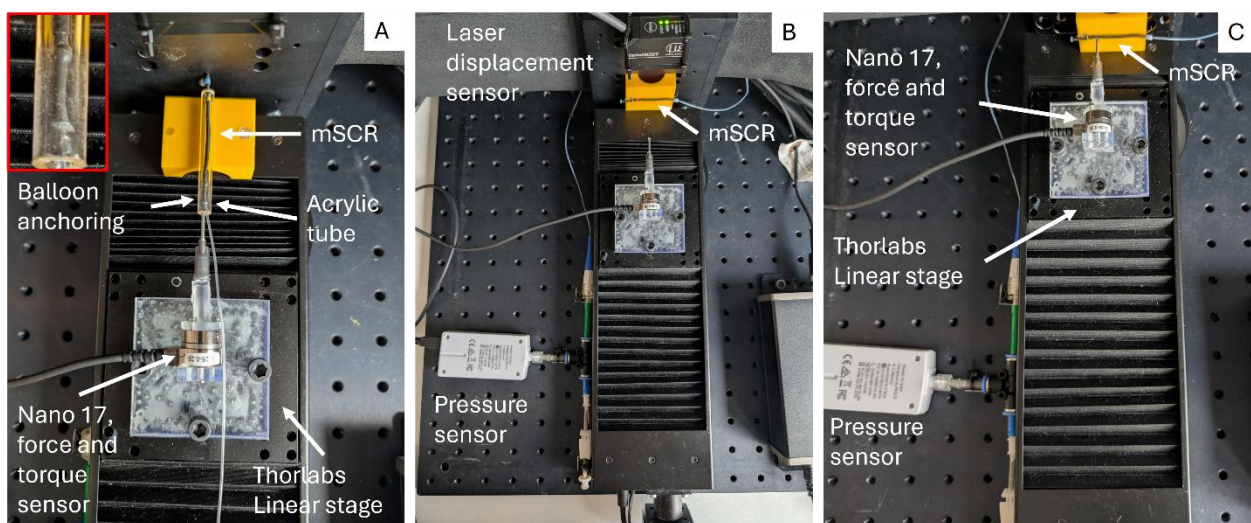
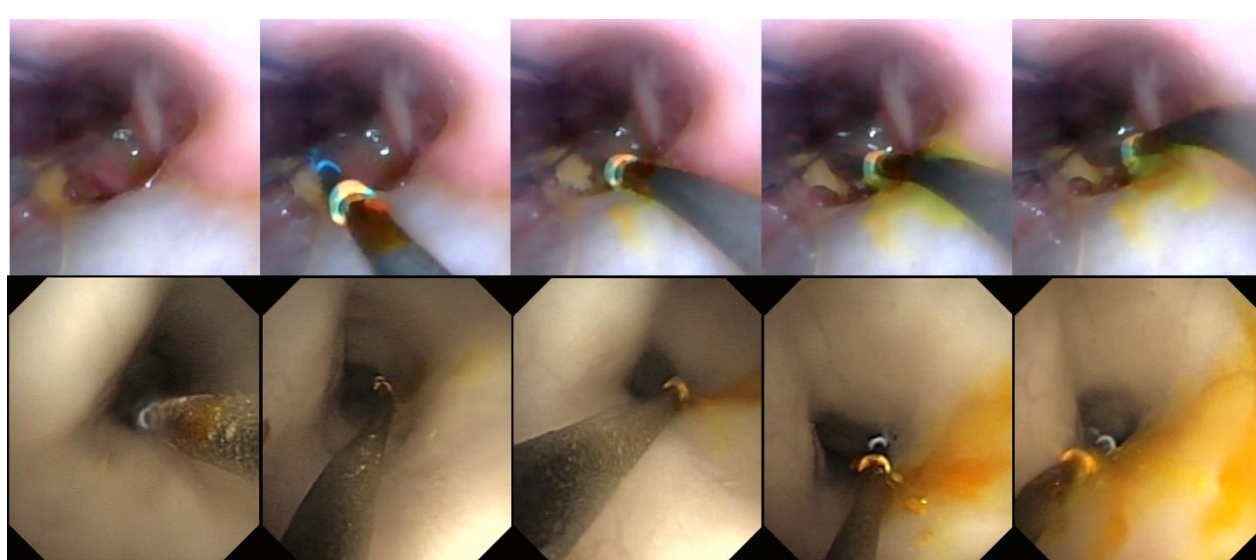
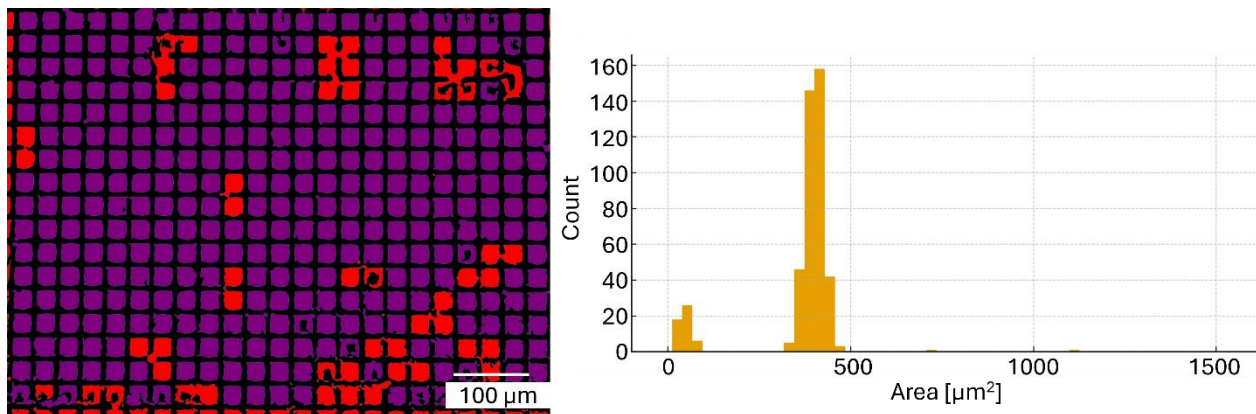


Figure S4 Demonstration of the conservation of the ability to perform shape forming using electromagnet platform (MiniMag, ETH [2]), while integration the magnetic balloon

[2] Kratochvil, B.E. et al. (2014). MiniMag: A Hemispherical Electromagnetic System for 5-DOF Wireless Micromanipulation. *Experimental Robotics. Springer Tracts in Advanced Robotics*, vol 79

Endoscope	Model	Organ	Test demonstration	Task
Duodenoscope	Olympus JF-130	Duodenum	In vivo	Human and autonomous cannulation of the papilla
Gastroscope	Olympus GIF-H180	Esophagus, Stomach, Duodenum	In vivo	Human and autonomous cannulation of the papilla. Gripper and drug delivery in different environment
Colonoscope	Olympus Cf-Q160	Colon	In vivo	drug delivery in different environment
Colonoscope	Olympus Evis X1 – CV1500	Duodenum	Ex vivo	Validation of the drug delivery tracking using narrow band imaging
Bronchoscope	Olympus, Q180-AC	Lung	In vivo	Navigation demonstration and drug delivery in different environment

Table S1 Standard medical endoscopes illustrating the cross-compatibility of our approach when applied in different settings



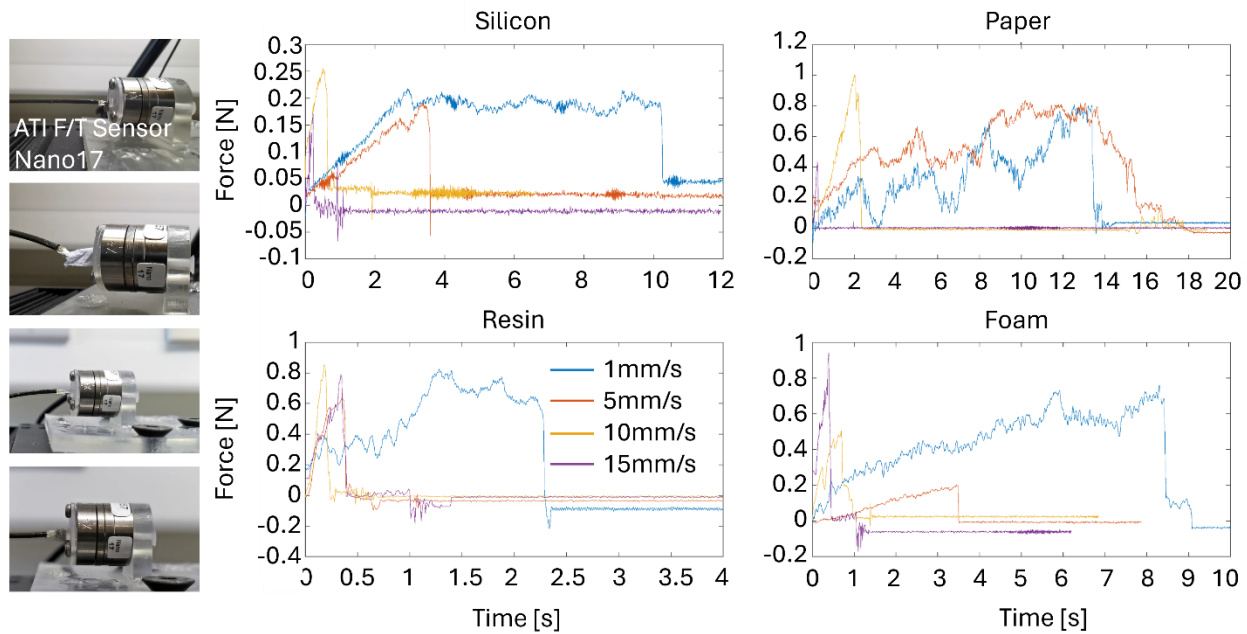


Figure S8 Validation of gripping performance on materials spanning different stiffness properties and tested at multiple movement speeds.

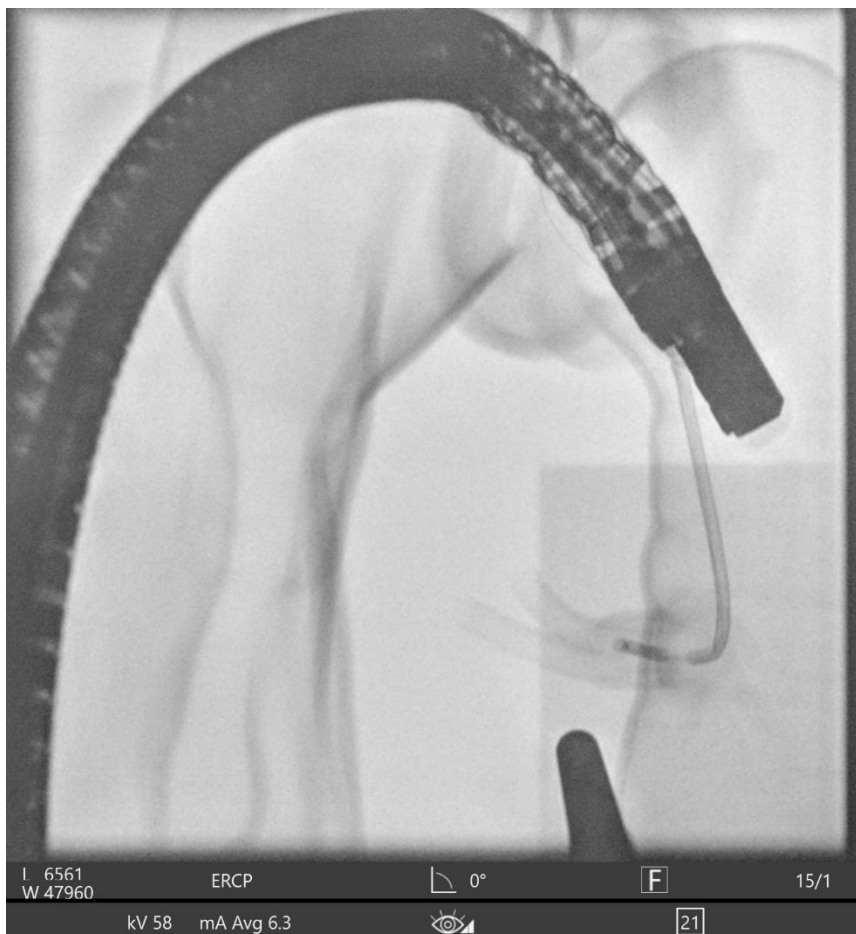


Figure S9 mSCR navigation visualized under C-arm fluoroscopic imaging (Omniscope Dream, Stefanix).

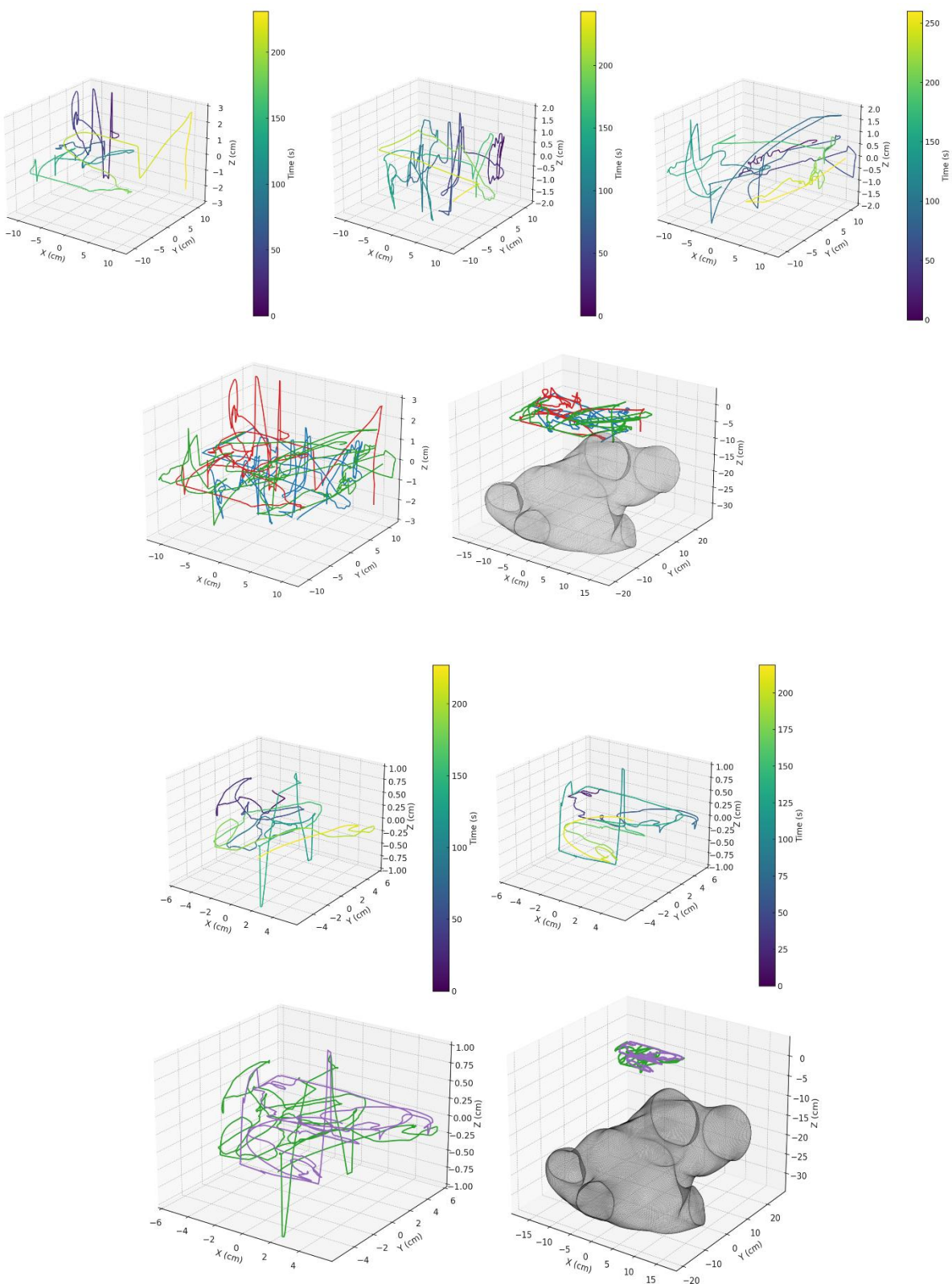


Figure S10 Details of the EPM trajectory illustrated in Figure 6.

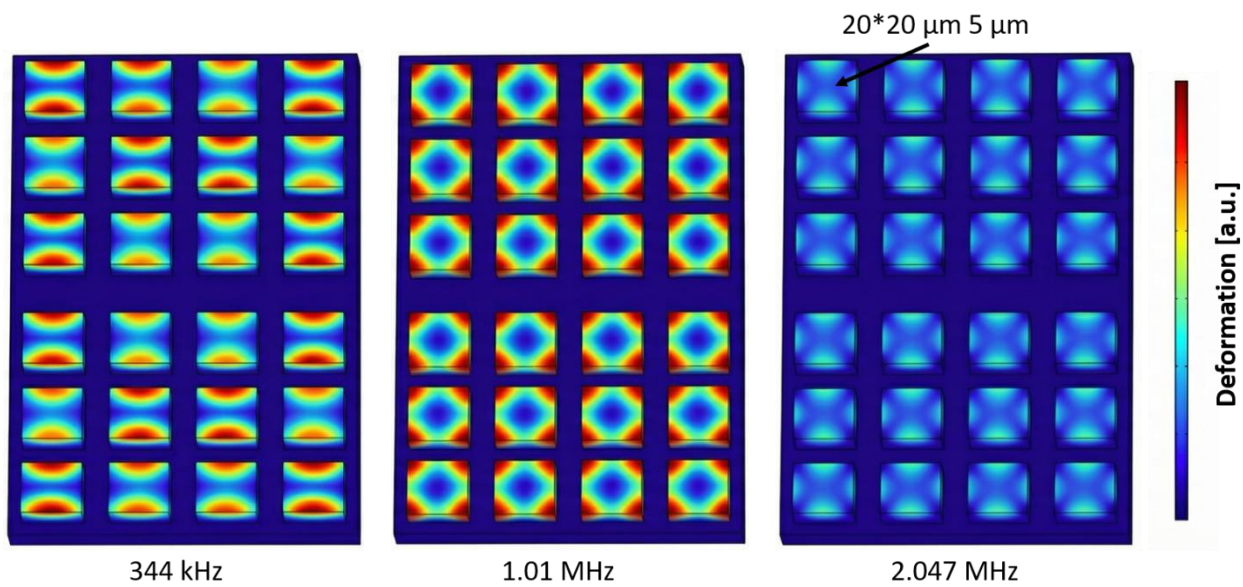


Figure S11 Finite Element Analysis results illustrating how the PLA shell pattern deforms as a function of the applied ultrasound frequency.